Axial and circumferential behavior of rock-socketed FRP-SSC composite piles monitored by distributed optical fiber sensors

by

Numan Malik (Ph.D. Candidate)
Department of Civil and Environmental Engineering, The Hong Kong Polytechnic University, Hong Kong, China. Email: numan.malik@connect.polyu.hk

Wen-Bo Chen (Ph.D., Professor)
College of Civil and Transportation Engineering, Shenzhen University, Shenzhen, China
Email: geocwb@gmail.com

Pei-Chen Wu (Ph.D., Research Assistant Professor, Corresponding Author)
Department of Civil and Environmental Engineering, The Hong Kong Polytechnic University, Hong Kong, China. Email: elvis.wu@polyu.edu.hk; peichen.wu@connect.polyu.hk

Ze-Jian Chen (Ph.D., Research Assistant Professor)
Department of Civil and Environmental Engineering, The Hong Kong Polytechnic University, Hong Kong, China
Email: zejchen@polyu.edu.hk

and

Jian-Hua Yin (Ph.D., Chair Professor)
Department of Civil and Environmental Engineering
Research Institute for Land and Space
The Hong Kong Polytechnic University, Hong Kong, China (Email: cejhyin@polyu.edu.hk

Manuscript to be submitted to *Journal of Geotechnical and Geoenvironmental Engineering* for possible publication as an original research paper
October 2024

Abstract

Traditional pile foundations in harsh marine environment may experience steel corrosion or concrete deterioration. Besides, conventional measuring devices like strain gauges and vibrating wire extensometers are sensitive to environment and only provide discrete strain data at certain points leading to inadequate information of the entire pile response. This study investigates an innovative and sustainable design of fiber-reinforced polymer (FRP) seawater sea-sand concrete (SSC) composite piles under static loading in physical model tests. Two rock-socketed model piles with different structural configurations, i.e., FRP rebars reinforced SSC and FRP tube confined SSC, were installed in the physical model tests. A fully distributed sensing method based on optical frequency domain reflectometry (OFDR) was used to measure the axial and circumferential strain profiles along the pile length. Besides, the displacement accumulation, end bearing pressure, and shaft friction mobilization within the rock-socket under static monotonic loading were analyzed and explored in detail. The test results indicated that the distributed axial strain profiles of both model piles appeared to follow similar trends along the depth with strain concentrations in one third region near pile head, which led to pile failure at that section. The continuous strain data enabled calculating reliable shaft friction values which showed maximum mobilization in the upper one third region of the socket. The distributed circumferential strain profiles along the pile length provided reliable information of the localized potential failures around the pile circumference, corresponding well with that from axial strain measurement. Finally, existing analytical solutions of partially embedded piles were adopted to describe the test results, showing good agreement of the test findings.

Keywords: Rock-socketed piles, optic fiber sensing, sustainable materials, shaft friction, distributed strain profiles

1 Introduction

Cast-in-place bored concrete piles socketed into rock with the applied load resisted by socket shaft resistance and end bearing resistance are widely used for bridges, high-rise buildings, and offshore structures. These piles provide versatile and sustainable foundation solutions due to high bearing capacity, minimal noise, less ground vibration, and high flexibility in length and diameter. Traditionally, the design of such rock socketed piles is based on one of the following four methods: empirical correlations based on unconfined compressive strength (UCS) of rock and concrete, shaft diameter, and socket roughness, standard code of practice, rational method based on settlement analysis and bearing capacity, or field static load tests (Zhan and Yin, 2000).

Many researchers have proposed empirical correlations predicting the shaft resistance of rock-socketed piles measured in static load tests. Field load tests on small diameter (200-610 mm) piles conducted by Rosenberg and Journeaux (1976) showed that shaft resistance is mainly dependent on bond strength of concrete rock interface and UCS of rock. In 1979, Horvath and Kenney reviewed 49 load tests of rock-socketed piles with diameters (between 410 to 1220 mm) conducted in UK, USA, Canada, and Australia, and observed that socket shaft resistance was fully mobilized at approximately 6 mm (0.5-1.5% of pile diameter) displacement. And they also correlated shaft resistance with UCS of rock. Furthermore, O'Neill et al. (1996) compared the empirical correlations based on UCS of weaker material (concrete or rock) developed by different researchers (Kaderabek and Reynolds, 1981; Williams and Pells, 1981; Rowe and Armitage, 1987; Carter and Kulhawy, 1988; Reese, 1988; Toh et al. 1989) with an international database of 137 rock socketed pile load tests and concluded that none of the correlations worked satisfactorily with the database results. Unlike previous empirical models, Seidel and Collingwood (2001) developed an analytical method for determining the shaft resistance of drilled and grouted piles socketed in rock, which was validated using extensive database covering a wide variety of rocks. This method incorporated major factors influencing shaft friction like socket roughness, rock mass stiffness, socket diameter, and normal stress at rock-concrete interface. However, quantifying the effect of construction techniques, effect of drilling slurries, debris smear, bonding type and drilling practices were not incorporated in developing the correlations that possibly influence the shaft friction mobilization.

The use of load-transfer curves based on maximum allowable settlement and bearing capacity provides an approach for the design of pile foundation, but remarkable experience and engineering judgment will be required to implement such curves in the field whose conditions differ distinctly with that where these curves were obtained (Gill, 1980; Mandolini et al. 2005; Lee and Park, 2008). Although fully instrumented static load tests recommended by standard design codes provide a rational design approach, it might be limited to high profile projects with sufficient budget in field testing (Zhan and Yin, 2000). Therefore, physical model tests were employed in this study to investigate the complex interaction between pile shaft and rock, identify potential design issues, and validate numerical models to be used for parametric studies in the future.

An efficient, cost-effective and sustainable foundation design method is required for long-term stability and performance of the structures. In contrast, traditional piling materials in harsh marine environment experience steel corrosion, timber degradation, and concrete deterioration, leading to huge maintenance costs and possibly structural failure (Krauss and Nmai, 1996). Besides, consumption of large quantities of river sand and fresh water in the construction industry posing threat to river ecosystems, increased flooding events, and depletion of natural resources (Xiao et al. 2017). Considering this, concrete structures using desalted sea-sand have been found in many countries including China, Japan and England. However, the salinity of seawater and sea-sand exaggerated the corrosion and degradation issues of traditional piling materials. Fiber reinforced polymer (FRP) materials have emerged as an attractive alternative to steel due to their high durability, anti-corrosiveness, light weight, low maintenance cost, and flexibility in design (Mirmiran et al. 1999; Fam et al. 2003; Sakr et al. 2004; Pando et al. 2006; Park et al. 2011; Zyka and Mohajerani, 2016). Therefore, seawater sea-sand concrete (SSC) reinforced with FRP composites provides an effective and sustainable approach for replacing traditional piling materials in marine environment.

Conventional measuring devices like strain gauges and vibrating wire extensometers provide discrete strain data at only certain points, which have limitations. Firstly, the shaft friction values calculated from strain profile and load distribution curves based on discrete point measurement data would differ from actual values. Secondly, using conventional sensors would suffer from cable congestion, high cost and data acquisition equipment constraints for offshore rock socketed piles which penetrate through the full depth of seawater. Thirdly, marine corrosive environment would be a challenge for the durability and functionality of these resistance-based sensors. Therefore, novel measuring techniques are required to measure reliable strain distribution and response of the piles.

Fiber optic sensing techniques have overcome the limitations of traditional sensors. These optic sensors provide distributed strain profiles, long sensing range choices, anti-corrosive, high spatial resolution, easy operation and installation, presenting a better pile monitoring solution. Many researchers have applied fiber optic sensors in monitoring geotechnical engineering applications like natural slopes, diaphragm walls, tunnels, pipelines, pile foundations, bridges, railway and road embankments, and dams (Iten et al. 2008; Hauswirth et al. 2014; Soga, 2014; Zhang et al. 2015; Schenato, 2017; Bersan et al. 2018; Pelecanos et al. 2018; Wu et al. 2021; Zheng et al. 2021; P. Wu et al. 2022; Lin et al. 2023). Fiber optic sensors include discrete sensors like fiber Bragg gratings (FBG) and distributed fiber optic sensing (DOFS) techniques like Brillouin optical time-domain reflectometry (BOTDR) and optical frequency domain reflectometry (OFDR). The BOTDR sensing technique uses typical spatial resolution of 0.5 to 1.0 m Compared to BOTDR, the OFDR sensing technique provides higher spatial resolution and faster data acquisition rate, facilitating real time monitoring of structural deformations with greater details. It is worth mentioning that data profiles provided by both BOTDR and OFDR can exhibit varying wavy nature, depending on the spatial resolution and sensing range. Therefore, appropriate filtering techniques may be necessary prior to data analysis (Pelecanos et al., 2018). Besides, as a newly developed distributed sensing technique, OFDR is rarely used for monitoring the piles except by Bersan et al. (2018) who applied DOFS for measuring axial strain of an augured cast-in-place pile at a relatively low spatial resolution of 10 mm. However, circumferential strain distribution of the pile provides a better understanding of the interactions between piles and surrounding soil. The presence of any voids, fissures, cracks, or any irregularity in pile body can influence the stress state surrounding pile, which can be detected through circumferential strain distribution curves. Furthermore, these curves can identify potential bending or lateral deformation of pile at certain points under axial load, high strain concentration positions, and variations in underlaying soil or rock layers conditions. Therefore, DOFS for axial and circumferential strain distribution is desirable, enabling engineers to understand the behavior of piles under different loading conditions and validate design and assessment analysis assumptions.

This paper investigates the behavior of the proposed sustainable design of FRP composites reinforced SSC model piles installed in the rock socket. Two different physical model piles: FRP rebars reinforced SSC model pile and FRP tube confined SSC model pile installed in rock socket were tested and the axial and circumferential strain distribution, displacement accumulation, end bearing pressure, and shaft friction mobilization under static monotonic loading were monitored. OFDR technique at a spatial resolution of 1mm and high sensing accuracy of ±1με was used for the first time to our knowledge for strain measurement. The monitored data from OFDR sensors are analyzed and compared to the data measured by FBG sensors (discrete sensing method). Advantages and applications of each sensing method are emphasized for future studies to advance pile monitoring practices. The test findings are compared with the analytical solutions of partially embedded piles and found to be in good agreement.

2 Methodology

2.1 Strain sensing principle of OFDR optic sensors

Among the DOFS techniques, OFDR is an advanced sensing method based on the principle of Rayleigh backscattering. The Rayleigh scattering light is quasi-elastic scattering light whose frequency will not drift during scattering in the fiber. When a small strain or temperature variation occurs in the fiber, it causes a change in refractive index inducing shift in the local spectrum. Fig.1 illustrates that when a light emits from a tunable laser source, it is divided into two branches (i.e., the reference light and measurement light) through an optical coupler. Rayleigh backscattered light is generated when the measurement light passes through measuring fiber and combines with the backscattered light from the reference branch creating an interference signal which can be detected and demodulated by optical detector. The Rayleigh backscattering spectrum shifts with the changes in strain and temperature of the optical fiber, expressed by the given relation:

$$\Delta v = C_{\varepsilon}\Delta\varepsilon + C_T\Delta T \tag{1}$$

where Δv is Rayleigh spectrum shift; $\Delta\varepsilon$ represent strain change; ΔT stands for temperature change; and C_{ε} and C_T are the strain and temperature coefficients, respectively. For standard single mode fiber with 1550 nm bands under Rayleigh backscattering, $C_{\varepsilon} \approx -0.15\ \text{GHz}/\mu\varepsilon$ and $C_T \approx -1.25\ \text{GHz}/\mu\varepsilon$ are normally used in OFDR system (Wu et al. 2020; Lin 2023). However, the coefficients may require calibration to account for the strain transfer effects, which can vary depending on factors such as fiber coatings and jackets, host matrix, and attachment or embedment methods (Li et al. 2010; Mohamad et al. 2010; Zhang et al. 2019; Lin 2023). The strain or temperature dependent spectrum can be calculated relatively between the reference signal (data measured under zero strain and room temperature condition) and measurement signal (data measured when strain or temperature changes). In this study the temperature change was neglected due to constant temperature conditions kept in the laboratory where tests were conducted.

In this study, OFDR based interrogator (OSI-I, Junlong Technology Ltd., China) was used. The interrogator operates in two different modes relying on the maximum length of fiber. In standard mode, it can provide strain reading at each 1 mm which is the spatial resolution for maximum 50 m length of fiber (sensing range). In long range mode, the spatial resolution of the interrogator reduces to 10 mm for the maximum sensing range of 100 m. For both modes, a high strain sensing accuracy of ±1 με can be achieved. The data acquisition rate depends on the sensing range of the fiber and required spatial resolution. For example, in 1 mm spatial resolution mode, the interrogator approximately takes around 6 seconds to sample strain data for 30 m length of the fiber. A smaller sampling time can be achieved by decreasing the length of fiber or by reducing spatial resolution. In comparison to various DOFS, the OFDR sensing technique offers higher spatial resolution and faster data acquisition rate, enabling real time monitoring of piles with greater detail.

2.2 Strain sensing principle of FBG optic sensors

The sensing principle of FBG optic sensors depends on the wavelength λ shift of the light that passes through the grating section of the fiber as shown in Fig. 2. A specific wavelength of light is reflected called Bragg's wavelength caused by the variations in strain and temperature of the optical fiber with correlation given as

$$\frac{\Delta\lambda}{\lambda_i} = c_1\Delta\varepsilon + c_2\Delta T \tag{2}$$

where i is the initial state; $\Delta\lambda$ stands for wavelength change; ΔT refers to temperature change; $\Delta\varepsilon$ denotes the change in strain; c_1 and c_2 are the coefficients of strain and temperature change, respectively. In this study, the value of c_1 was taken as 0.78 whereas temperature change was neglected due to constant temperature conditions in the laboratory (Pei et al. 2014). In this study, FBG interrogator named SM130 from MICRON OPTICS was used. SM130 sensing interrogator features a very high power, low noise swept wavelength laser realized with Micron Optic patented Fiber Fabry-Perot Tunable Filter technology.

2.3 Design of the model piles

The model piles were constructed in a physical model, specially designed, and built for this study in the Soil Mechanics Laboratory of The Hong Kong Polytechnic University, as shown in Fig 3. A hydraulic loading actuator (GCTS, USA) that is capable of applying static and cyclic loads was supported by a specially designed steel reaction frame. A steel tank with an inner diameter of 1000 mm and inner depth of 1326 mm was designed for the construction of model piles. A granite rock socket of certain roughness was drilled with depth of 160 mm and diameter of 100 mm. In the field applications of many regions (e.g. Hong Kong), rock socketed piles normally have a diameter of 1-2m and depth of 0.5 to several meters in the rock (Ng et al. 2001). The socket length-diameter ratio is 160/100=1.6 in this study and is within a common range of engineering practice. In order to position the granite rock in the center, a layer of hardened gypsum was laid at the bottom of the steel tank.

Both the model piles have similar diameter of 100 mm, and length of 1460 mm of which 160 mm was embedded in the socket and 1300 mm was above the rock surface. Pile I was constructed from SSC reinforced with four GFRP rebars as illustrated in Fig. 4. Circular GFRP stirrups were used to confine four GFRP rebars, which had a diameter of 9.5 mm and a length of 1460 mm. The stirrups were placed at center to center spacing of 70 mm along the pile's length from top to the rock surface. The rebar cage was first fabricated and fixed in the rock socket. The polyvinyl chloride formwork provided casing and the SSC was cast within it followed by curing for 28 days. According to the manufacturer report, the rebars were made from unsaturated polyester resin and E-glass fiber coated with sand possessing elastic modulus of 50.8 GPa. Pile II was constructed from SSC confined with GFRP tube (wall thickness of 3.5 mm) with inner diameter of 100 mm and length of 1300 mm as shown in Fig. 5. The SSC was confined with GFRP tube above the rock surface only. For the construction of the model pile, SSC was cast directly inside the rock socket and in the GFRP tube which worked as permanent casing. The GFRP tube was produced from E-glass fiber and vinyl ester resin under filament winding process with fiber orientation of ±45º. The axial and hoop moduli of 11.3 and 10.1 GPa, respectively, were obtained from compression tests of small specimens (height of 60 mm and thickness of 3.5 mm) cut from GFRP tube.

A specially designed mix ratio of SSC with ingredients of seawater, sea sand, cement, fly ash, and superplasticizer was used for the construction of both model piles. Uniaxial compression tests were carried out on triplicate cylindrical specimens (height of 100 mm and diameter of 50 mm) of the SSC mix showing an average compressive strength of 35 MPa.

2.4 Installation and instrumentation of OFDR optic fibers and FBGs in the model piles

The effectiveness of an optical fiber sensor to monitor strain profile of a structure is based on the bonding properties and bonding method between the structural material and the optical fiber. Optical fibers have the capability to be embedded within the structural material, like reinforced concrete section, or attached to the surface of structure using adhesives. In this study, optic fibers were embedded within the concrete and FRP, as well as attached to the surface using an ultra-high-strength epoxy adhesive to protect the fibers and ensure a good bond between the fiber and surface. A single mode silicon optical fiber coated with PVC having diameter of 1.8 mm (manufactured by YOFC Ltd., Wuhan, China) used by Hong et al. (2016) and Wu et al. (2022) was used in this study.

Both the model piles were instrumented with OFDR and FBG optic fibers to monitor the behavior of piles. For Pile I, two independent OFDR optic fibers were installed on the rebars and within SSC along the length of pile, however, one fiber was damaged during the test preparation. The optic fiber has six sections (S1 to S6) for monitoring the strain of different locations of pile axially, as shown in Fig. 4(b). Additionally, eight OFDR optic fiber sections (S7 to S14) as shown in Fig. 4(a) were installed around the circumference at different positions at certain spacings along the depth of pile for monitoring the circumferential strain distribution. The longitudinal OFDR optic fibers attached to the rebars were glued within a notch of 3 mm depth on rebars while circumferential optic fibers were glued on the surface of concrete. Arrays of multiplexed FBGs were attached to the rebars as shown in Fig. 4(b). Eight FBGs were placed in the pile body above rock surface at a spacing of 160 mm and four FBGs within the rock-socket at a spacing of 35 mm.

For Pile II, one OFDR optic fiber was installed along the length of pile with six sections embedded at different positions. Four sections (S1, S9, S10, and S11) were placed longitudinally along the interface of FRP and SSC and two sections (S5, S6) were embedded within the SSC monitoring the strain at different positions of pile as shown in Fig. 5(b). Additionally, seven OFDR optic fiber sections (S2 to S8) as shown in Fig. 5(a) were installed horizontally on the outer circumferential surface of GFRP tube along the length of pile, monitoring the hoop strain distribution at different positions. An array of quasi-distributed FBGs was attached to the long aluminum channel with U-shaped cross section and placed within the SSC as shown in Fig 5(b). The aluminum channel was used to protect the vulnerable FBGs array while casting the concrete and to form a quasi-distributed sensing strip along the length of pile. Eight FBGs were installed in the pile body above the rock surface and four within the rock-socket at spacing of 160 mm and 35 mm respectively.

For both piles, the measuring OFDR optic fibers were first pre-tensioned by 50 to 100 micro strain, before being glued on the structural surface. The purpose of pre-tensioning fiber was to ensure that it is in a known and stable state of tension prior to loading, thereby preventing unintentional changes in the position of fiber during casting concrete. To avoid imperfect strain transferring near the measuring fiber boundary and increase effective measuring fiber length, an additional 25% fiber length of the pile diameter was bonded for circumferential optic fiber sections (Lin et al., 2021). Additionally, the thickness of the adhesive layer was kept uniform and thin for reliable strain data. The whole length of the OFDR optic fiber worked as a distributed sensor, hence certain sections of the fiber were kept free in the air, called slack fiber section, for locating the measuring fiber sections along the length of fiber.

2.5 Analysis of sensing data from optical fibers

The data measured consists of strain along the whole length of the fiber with a spatial resolution of 10 mm, using OFDR sensing technique discussed in section 2.1.

The geotechnical parameters of the pile can be calculated based on the strain profiles measured with OFDR fiber optic sensors. The following relations were used to determine pile shaft resistance-compression (f - u) curves within the rock-socket:

$$u(y) = \int_0^l \varepsilon(y)dy \tag{3}$$

where $u(y)$ represents the accumulated compression within the rock-socket starting from pile base; l shows the depth of rock-socket; $\varepsilon(y)$ stands for the measured strain along the depth within the socket at a distance of y from pile base. The shaft resistance f is given as

$$f(y) = \frac{dF(y)/d(y)}{\Delta h \cdot \pi \cdot D} \tag{4}$$

where D is the pile diameter; Δh is the distance between two strain measuring points and $dF(y)$ is the force difference between two consecutive surfaces with distance of Δh , and the force applied on the cross-section can be determined by

$$\frac{dF(y)}{d(y)} = A\varepsilon(y)\frac{dE(y)}{d(y)} \tag{5}$$

where EA is the axial rigidity of pile (E is the Young's modulus and A is the cross-sectional area). The Young's modulus of the pile was determined from the moduli of the materials used in the pile (i.e FRP and concrete) given as

$$E = \frac{E_c A_c + E_f A_f}{A_c + A_f} \tag{6}$$

where E_c and E_f are the moduli of concrete and FRP respectively; A_c and A_f represents the area of the concrete and GFRP respectively. The GFRP rebars were considered as linear elastic materials with an elastic modulus of 50 GPa. However, the concrete was considered a non-linear elastic-plastic material and the stress-strain curve measured by strain gauges of small cylindrical specimens fitted well with the equation specified in Comite Euro-International du Beton–Federation International de la Precontrainte (CEB-FIP) Model Code (FIP 1993) :

$$\frac{\sigma_c}{f_{cm}} = \frac{A\eta - \eta^2}{1+(A-2)\eta}, \eta = \frac{\varepsilon_c}{\varepsilon_{cm}}, A = \frac{E_c}{f_{cm}/\varepsilon_{cm}} \tag{7}$$

where σ_c represents axial stress; f_{cm} stands for the peak stress (f_{cm}= 31 MPa); ε_c refers to axial strain; ε_{cm} denotes the strain at f_{cm} (ε_{cm}= 0.00344); E_c is the initial elastic modulus (E_c = 22.9 GPa). The tangent modulus $E_t = \dfrac{d\sigma_c}{d\varepsilon_c}$ varied according to Eq. (7), which was used for calculating the load distribution of piles.

3 Results of Pile I - FRP rebars reinforced pile

3.1 Axial Strain profile along the depth of the pile

Fig. 6(a) shows the axial strain profile measured by OFDR and FBG optical fibers at different loading levels along the length of pile. Compressive strain is characterized as negative and tensile strain is positive in this study. The axial strain by OFDR is calculated as the mean value from the two fibers in the pile body (S1 and S3) glued on two different rebars as shown in Fig. 4(b). Similarly, the FBG data is the mean strain measured by two arrays, each glued on different rebars. The strain was measured at a spatial resolution of 10 mm by OFDR optic sensors along the depth. It is observed that in Fig. 6(a), the strain profile measured by both OFDR and FBG were generally in good agreement with one another. The strain measured with OFDR optic fibers is relatively lower than that of FBGs which could potentially be attributed to (i) the strain transfermechanism of different optical fibers and (ii) slight eccentricity. One may notice that the mean center of S1 and S3 was not at the center of the cross-section of the pile, whereas the mean center of FBGs was positioned at the center. The difference in strain responses at the same depth but at different positions across the cross-section of the pile can reveal the effect of eccentricity on strain localization, which can be also seen from circumferential measurements in Section 3.3.

Fig. 6(b) presents the overall integrated axial strain measured by OFDR and FBG optic fibers at different loading levels against the LVDT data. The OFDR strain value at a specific depth is the mean strain of six fibers at the same level. The average of the results measured by two LVDTs fixed at the pile head is calculated and presented in the Fig 6(b). It can be seen that the strain measured by both OFDR and FBG optic sensors have almost similar trends with that calculated from LVDTs. However, the OFDR strain data exhibited a higher correspondence with the data from LVDTs. In addition, the OFDR sensing technology provides distributed sensing, giving more reliable data for analysis like necking, localized deformations, and cracks monitoring whereas such localized features would not be monitored by discrete sensing methods like FBGs or vibrating wire strain gauges. Therefore, this study will primarily discuss the OFDR sensing data to investigate the response of the model piles.

The strain distribution monitored with OFDR optical fiber sections (S1, S4, S5, and S6) along the pile length under different monotonic load levels are shown in Fig. 7. There is no surrounding soil around the pile body making the axial load constant above the socket, and hence the strain was generally uniform from top to the rock surface under 30 kN and 60 kN load levels. However, between 200 to 400 mm, the strain response measured by the four fiber sections showed higher localized strain values, which were clearly observed in the form of cracks at higher load levels during failure of the pile. The strain increased with increase in load with maximum strain values measured at maximum load 213 kN. The strain profile monitored by different fibers showed different types of curves. The fiber glued within the notch on the rebar recorded smoother strain curves under different loading levels as shown in Fig. 7(a). The rebar provided a substrate with uniform modulus, enabling the fiber to record smoother strain data.

However, the fiber sections placed within the concrete showed obvious wavy strain curves, as shown in Figs. 7(b), 7(c), and 7(d) due to the presence of stirrups. The lateral FRP reinforcement in the form of stirrups was placed at approximately 70 mm spacing, with adjustments made to facilitate the installation. The stirrups provided lateral confinement; hence the fiber measurement points in contact with stirrups have higher strain values compared to the fiber section in between, which produced wavy strain profiles. Generally, under the axial load, the concrete expands laterally which is restrained by the FRP, hence the FRP experiences higher strain due to confining effect. When the axial load increases, the confining action of the FRP increases, which was confirmed by the OFDR optical fibers strain profile seen in Figs. 7(b) and 7(c). From 1300 to 1450 mm is the socket, and the strain profile has smooth curves for all the fibers due to the absence of lateral FRP stirrups and high confinement effect from rock socket. The strain decreased monotonically along the depth due to the shaft resistance within the socket portion.

The strain profile measured by different fiber sections at peak load of 213 kN is shown in Fig. 7(e). The fiber section S1, showed a smooth strain profile compared to the other fiber sections due to its placement on a FRP rebar with uniform modulus along the depth. The other fiber sections except S4 were attached to the ties longitudinally, therefore the profile recorded by these fibers is wavy, indicating peaks at position where the fiber in contact with FRP stirrups and valleys showing the portion in concrete. The fiber section S6 outside the rebar cage in concrete cover showed higher strain values due to no confinement from FRP. The strain within the region 200 to 400 mm showed a sudden increase indicating the weaker portion, which was confirmed by cracks in this region during failure of pile and will be shown in later sections. The strain within the socket followed a smooth decreasing trend along depth and all the fiber sections recorded the same values of strain approximately.

3.2 Mobilized shaft friction in the rock socket

Shaft friction profiles at different loading levels were calculated using Eq. (4) based on the strain profiles measured by different fiber sections. According to Eq. (6) the modulus of the pile can be calculated based on the moduli of FRP and concrete, hence fiber sections (S1 and S3) attached to independent longitudinal FRP rebars and one fiber section (S4) embedded in the concrete were considered for determining shaft friction profiles development. The curves in Fig. 8(a) show the mobilized shaft friction profiles under different loading levels measured with different fiber sections along the depth within the rock socket.

Generally, the shaft friction decreased along the depth for the same loading magnitude and increased with increase in loading level. The maximum shaft friction of 5.5 MPa under 213 kN was mobilized in the region of 0-20 mm and dropped to 4 MPa in the region of 20-40 mm and decreased slowly along the depth under the same load. The shaft friction profiles showed smooth curves which can be used for evaluation and determination of mean shaft friction for the predictive and design tools. The variation of mean shaft friction and end bearing pressure with the applied load based on the average strain data from fiber sections S1, S3, and S4 are shown in Fig. 8(b). The mean shaft friction increased almost linearly with load, while the end bearing had a non-linear response, that might be induced by the initial contacting and conditioning process between pile end and rock. Under a load of 213 kN, the mean shaft friction reached a maximum of 3.3 MPa with an end bearing of 4.85 MPa. The shaft resistance mobilized early at smaller displacement and linearly increased to a maximum of 178 kN resistance under 9 μm as shown in Fig. 8(c). However, the base resistance mobilized at higher displacement comparatively showing a maximum value of 45 kN at 9 μm. The base resistance showed a non-linear response and increased at higher rate when the displacement increased beyond 3 μm. The maximum resistance was provided by the pile shaft compared to the base, accounting for approximately 80% of the total resistance. These findings are consistent with the field design approach proposed by Haberfield and Collingwood (2006) and with the field load tests results of drilled shaft foundations socketed into rock (Carter and Kulhawy, 1988).

3.3 Circumferential strain distribution

The circumferential strain distributions monitored by four independent OFDR fiber sections (S8, S9, S12, and S14) around the pile circumference at different positions are shown in Fig. 9. The strain distribution run in the clockwise direction from 0° to 360° around the circumference of pile. The 0° position on pile circumference represents the actual North (N) direction in the laboratory, whereas 90°, 180°, and 270° positions refer to East (E), South (S), and West (W) directions, respectively. The 0° to 360° represents the circumferential length of pile (0 to 360 mm) and was presented in the form of angular directions for clear illustration. The tensile strain is positive which is similar to OFDR interrogator default measurement sign. In general, the shape of strain profiles for different OFDR optical fiber sections placed at different positions varied.

The circumferential strain distribution measured with the fiber section S8 under different load levels is shown in Fig.9(a). The strain distribution around the circumference fluctuated and showed higher strain values in the region between 240° to 260° mm and 320° to 350°. Under different loading levels, the strain distribution pattern around the circumference remained the same, but the strain values increased with the increase in load.

Fig. 9(b) shows the hoop strain distribution at the position of 400 mm from the pile head, monitored by fiber section S9 around pile circumference under different load levels. The strain distribution around the circumference showed a uniform pattern. However, a sudden increase in strain appeared in 210° to 280° region. This variation in the pattern can be attributed towards the strain localization towards the southwest side of the pile. The circumferential strain profile remained the same for different loads and increased with load level. The fiber section S12 at the position near the position of 800 mm from the pile head, monitored the circumferential strain distribution as shown in Fig. 9(c). The hoop strain profile around the circumference of pile varied in southwest and northwest side, showing maximum strain values between 0° to 40° and 210° to 320° regions. The strain pattern remained the same for different loads and with increase in load strain values increased. The distribution of the circumferential strain confirms the effect of eccentricity on strain localization at a depth of 800 mm of the pile observed in Section 3.1.

Similarly, the circumferential strain monitored by the fiber section S14 at the position of 1100 mm from the pile head is shown in Fig. 9(d). The strain profile around the circumference showed uniform pattern approximately with fluctuations in strain appeared between 30˚ to 60˚ and 250˚ to 290˚ mm regions. The maximum strain was recorded on the west side of the pile, corresponding to the strain localization in this region.

3.4 Comparison of axial and circumferential strain localizations with failure mode

The distribution of the axial strain along pile length and hoop strain around the circumference of the pile at failure stage is shown in Fig. 10. Three distributed fiber sections (S1, S3, and S5) present the axial strain response and five representative distributed circumferential fiber sections (S8, S9, S12, S13, and S14) presents circumferential strain distribution. The localized strain concentrations were successfully monitored by both axial and hoop optic fibers which is the primary concern of this study. The observed cracks at failure stage between 200 to 400 mm and 900 to 1100 along the depth were clearly detected by the optic fibers which are consistent with the monitored strain profiles in Sections 3.1 and 3.3. The localized strains and failure in the one third region of pile length near pile head and pile base, indicate Euler second buckling mode as shown in Fig. 10. Besides, SSC was poured directly from the pile head into tubular mould which could have created a potential concrete density gradient, leading to non-uniform material compaction and possibly caused higher strain concentrations near the pile head.

4 Results of Pile II - FRP tube confined pile

4.1 Axial Strain profile along pile length

The axial strain profiles of FRP tube confined pile monitored by OFDR and FBG optical fibers at various load levels along pile length are shown in Fig. 11(a). The OFDR optic fiber strain profile was monitored by the fiber S12 embedded in the concrete at the same position as of FBGs. While the FBGs strain profile was developed based on the data monitored by FBGs array attached to the aluminum channel at the same position as S12, as shown in Fig. 5(b).

Both the distributed (OFDR) and discrete (FBG) sensing technologies showed similar strain profiles and generally were in good agreement with one another. The slight difference might be attributed to the strain transfer mechanisms of the different optical fibers. It should be mentioned that the FBG and OFDR fiber protective coatings have different mechanical properties which influenced the strain transfer from the substrate to the core of the respective optic fiber. Further investigations are needed to quantify the effects of strain transfer. Fig. 11(b) compares the axial strain measured by OFDR and FBG optical fibers at various loading levels to the strain data from LVDT. The OFDR sensing strain represents the mean strain of five fibers along the length of the pile. Similarly, FBGs strain data indicates the mean strain of twelve FBGs placed along the depth of pile on aluminum channel. The strain of LVDT was back-calculated from the mean displacement of two LVDTs positioned at the pile head. As found for Pile I measurement, the OFDR optic fibers data showed better agreement with LVDT results with higher level of linearity and similar coefficients.

Fig. 12 presents the strain profiles monitored by four independent OFDR fiber sections (S1, S9, S11, S12) along the pile length under different load levels. As shown in Fig. 5(b), three of the sensing fibers monitored the strain profile at the interface of FRP tube and concrete and one fiber section within the concrete. Similar to the previous pile, the pile stiffness was constant above the socket because of no surrounding soil. Hence the strain profile was generally uniform from pile head to rock surface and decreased monotonically within the socket due to shaft resistance. However, the strain response monitored by the four fibers in Figs. 12(a), 12(b), 12(c), 12(d) and 12(e) between 200 and 400 mm exhibited larger localized strain values, which were clearly evident in the form of FRP tube buckling and concrete cracks at higher load levels during failure stage. The strain values monitored by fibers of S1, S11 and S12 showed smooth profiles, while the fiber S9 recorded some abrupt strain variations between 570 to 670 mm. This variation could be caused by the improper attachment of fiber onto FRP tube, resulting in irregularity and unreliable strain transformation. The fibers placed at the interface of concrete and FRP tube showed higher strain values because of the confinement action of FRP tube. The lateral expansion of the concrete under axial compression was restrained by the FRP tube by providing confinement and recorded higher strains. However, the fiber section S11 embedded within the concrete monitored relatively small strain values. The strain increased consistently with increasing load, with maximum strain values observed at maximum load 266 kN, as shown in Fig. 12(e). The pile experienced buckling between 200 to 400 mm near the pile head, resulting in positive strain on the tension side as monitored by S10, and negative strain on the compression side as monitored by S11. The only fiber section S12 which monitored the pile socket strain distribution, showed a smooth decreasing trend between 1300 to 1460 mm because of shaft friction.

4.2 Mobilized shaft friction in the rock-socket

The strain profile monitored by the OFDR fiber section S12 embedded in the concrete was utilized for calculating the load transfer curves. The load-transfer curves were used for the calculation of mobilized shaft friction within the socket using Eq. (4) given in section 2.5. The fiber section monitored the strain till 120 mm depth of the socket, and beyond it the fiber was not able to detect the signals due to fiber sharp angle at the base within the socket. The shaft friction profiles at different loading levels along the depth within the socket are presented in Fig. 13(a). In general, shaft friction increased with increasing loading level and decreased along depth for the same loading magnitude. Higher shaft friction mobilization took place in the socket's upper region (0–50 mm), relative to the lower portion due to the small strain values near the base. Under the loading of 266 kN, the maximum shaft friction of 5.6 MPa mobilized in the 0–20 mm zone. The shaft friction decreased to 4.68 MPa in the 40–50 mm region and followed by a faster decreasing rate along the depth reaching 0.9 MPa near the base for the same load.

The mean shaft friction and bearing pressure evolution with the applied load are shown in Fig. 13(b). The mean shaft friction was calculated based on the shaft friction profiles calculated from the optic fiber data discussed in the previous section. The mean shaft friction showed approximately a linear response with the applied load reaching ultimate value of 4 MPa under the applied load of 266 kN. The rock socket used in this study had higher stiffness, therefore the mean shaft friction increased linearly at uniform rate. However, the end bearing pressure showed a nonlinear response comparatively and reached an ultimate value of 5.5 MPa. The mobilization of shaft and base resistance with the displacement at the upper cross-section of the socket near rock surface is presented in Fig. 13(c). The shaft resistance mobilized early at small displacements and increased linearly, providing around 77% contribution to resist the applied load. In contrast, the base resistance mobilized slowly at higher loads, reaching a maximum value of 52.7 kN when the displacement reached 9.5 μm. The base resistance accounted for around 23% of the applied load at the ultimate loading conditions.

4.3 Circumferential strain distribution

The circumferential strain distributions monitored with OFDR optic fiber sections (S2, S5, S7, and S8) around the FRP tube confined pile at different positions along the depth are shown in Fig.14. The strain distribution notations and signs are presented in Section 3.1 and 3.3.

Fig. 14(a) shows the circumferential strain distribution at the position of 200 mm from the pile head monitored by the fiber section S8 around the pile circumference under different loading levels. The strain values appeared higher between the north and west sides compared to the other directions with a peak tensile strain of 2500 $\mu\varepsilon$ under 180 kN. At failure stage, the pile bent in the region (200 to 400 mm along the depth) towards west side, creating compression in the FRP tube on the westside and tension on the east side as shown in Fig. 15. The higher strain on compression side is attributed towards the bulging of FRP tube and fiber matrix rupture, resulting in higher tensile stress in the circumferential fiber section. Under different loading levels, the stain contour remained the same in shape, but expanded in size with increasing load.

The circumferential strain distribution measured with the fiber section S7 placed at 400 mm around the circumference from the pile head is shown in Fig. 14(b). The strain values appeared higher on the west side of the pile cross-section comparatively. These strain localizations were observed in the form of FRP tube buckling as discussed previously with tension and compression along the east and west sides respectively shown in Fig. 18. The strain pattern remained the same for different loads, but strain increased with an increase in load.

The fiber section S5 placed near the middle of the pile length monitored the circumferential strain distribution as presented in Fig. 14(c). The strain profile showed uniform pattern radially, however, the strain values recorded were lower compared to other hoop sensing fiber sections. The circumferential strain monitored at 1100 mm depth from the pile head with fiber section S2 is shown in Fig. 14(d). The higher strain values appeared in the southeast side comparatively. This strain concentration could be attributed to the Euler deflection behavior of the pile as a column with one end (restrained to rotation and allowed to axial translation) and other end fixed support (under compression, the pile head acted as a support with no rotation but allowed to axial translation and the socket provided a fixed support to the pile).

4.4 Comparison of axial and circumferential strain response

The distributions of the axial strain along the pile depth and its circumferential strain at failure stage are shown in Fig. 15. The axial and circumferential fiber sections were aligned in cardinal directions (N, E, S, and W) in similar manner as discussed for Pile I in Section 3.1 and 3.3. The pile failed as a result of buckling and localized strains between 200 to 400 mm near pile head. The compression side of the buckled tube showed higher strain values due to FRP fibers and matrix damage which caused higher tensile strain concentration compared to the tension side. The strain localization was also observed between 900 to 1100 mm along the depth by circumferential fiber sections indicating Euler second mode buckling shape as shown in Fig. 15.

5 Comparison with analytical solutions

The physical model piles in this study are considered as partially embedded piles, where the load is transferred to rock base through shaft friction in rock socket and serve as a column for the portion above the rock surface. The pile head was restrained to rotation but allowed for axial translation by the load transferring plate shown in Fig. 3, while the pile bottom can be defined as fixed end due to the restraints of rotation and translation. However, the pile depth below the rock surface needs to be defined where it can be considered as fixed. This depth to fixity were predicted using analytical models which were derived using elastic Winkler foundation (Hetényi and Hetbenyi, 1946; Davisson and Robinson, 1965; Prakash, 1987; Heelis et al. 2004). The basic equation which defines moment equilibrium for partially embedded piles as

$$EI\frac{d^4x}{dy^4} + \left[P - \int_0^y f(y)dx\right]\frac{d^2x}{dy^2} - f(y)\frac{dx}{dy} + kx = 0 \tag{8}$$

where I is the moment of inertia of pile cross section, P is the axial compression applied at the pile head, x is the lateral deflection, $f(y)$ is the shaft friction along the depth y and k is modulus of subgrade reaction. k can be defined as $k = n_H y$. For granular soils, the k varies along the depth y, however in this study k is constant for rock mass hence $k = n_H$ and can be found as

$$k = n_H = \frac{E_m}{h} = \frac{0.5\sigma_c MR}{h} \tag{9}$$

where E_m and σ_c is the modulus of deformation and UCS of rock mass respectively. MR is the modular ratio and h is the height of rock specimen. The value of $k = 0.21$ GPa/mm was found for the granite rock specimens from UCS tests based on ASTM C469. Davisson and Robinson (1965) proposed a solution for a partially embedded pile utilizing non-dimensional parameters where length of pile below rock surface, $Z_{\max} = L_b / T$, depth to fixity, $S_T = L_{b'} / T$, and column length above the rock surface, $J_T = L_u / T$, where $T = \sqrt[5]{\frac{EI}{n_H}}$, and $L_{b'} = 2T$. Fig. 16 shows the equivalent embedded length ($L_{b'}$) of pile, where the total equivalent length is $L_e = L_{b'} + L_u$. The critical buckling load is then given as

$$P_{cr} = \frac{\pi^2 EI}{c\left(S_T + J_T\right)^2 T^2} \tag{10}$$

Since the pile cross-sectional area A and radius of gyration r are constant, the critical buckling load may be computed by using Euler's formula for slender columns given as

$$P_{cr} = \frac{\pi^2 EA}{c\left(L_e / r\right)^2} \tag{11}$$

where c is the factor for unembedded pile end condition and is calculated as 0.25, 0.49, and 1 for fixed, pinned and translation-no-rotation respectively, using Euler formula, with the embedded end considered as fixed.

The experimental test results of both the model piles were compared with the above analytical solutions. The flexure rigidity EI of Pile I and Pile II determined from the optic fibers monitoring in the static compression tests were 6.4×10^{10} Nmm^2 and 8.6×10^{10} Nmm^2 respectively. The maximum load sustained by Pile I and Pile II under static monotonic compression test was 213 kN and 266 kN respectively. The theoretical buckling loads for both the model piles were calculated with embedded and unembedded ends considered as fixed and translation-no-rotation and end of fixity taken at pile base in rock-socket. The Davisson and Robinson (1965) analytical approach in Eq. (10) predicted 252 kN and 340 kN buckling loads for Pile I and Pile II, showing approximately 15% and 21% difference between the predicted and test results respectively. The difference in results shows good correlation for the model piles tests and can be explained from the monitored strain profiles of both piles. The higher localized strain concentrations between 200 to 400 mm depth monitored by distributed optic fiber sections shown in Figs. 7 and 12 reduced the ultimate load carrying capacity of the piles. The localized strain concentrations can be attributed to reduced pile stiffness in this region due to low end fixity condition, degradation of modulus of pile due to pre-cyclic loading tests, and possibly low SSC density. The presence of the high localized strain values were monitored at the early stage under low load levels and hence were clearly observed in the form of cracks at higher load levels during failure of the piles.

Under the same end conditions and fixity depth as above, the Euler formula in Eq. (11) predicted 295 kN and 401 kN buckling loads for Pile I and II, showing approximately 27% and 33 % difference between the predicted and test results respectively. As discussed previously, the difference in results can be attributed to localized strains, true mode shape prediction, and reduced pile stiffness at certain points.

Both the model piles failed under Euler 2nd mode of buckling, with Pile II showing higher ductility comparatively. The Pile I failed due to the breakage of FRP rebars with obvious cracks, spalling and debonding of concrete from rebars as shown in Fig. 10. For Pile II, FRP tube provided better confinement effect, restrained concrete more uniformly and controlled the cracks propagation comparatively and failed due to the rupture and squeezing of FRP tube after full strain development shown in Fig. 15.

6 Conclusions

This paper analyzed the axial behavior FRP rebars reinforced and FRP tube confined SSC model piles installed in rock-socket through physical model tests. A distributed sensing technique, i.e., distributed OFDR sensors, was employed to monitor the fully distributed axial and circumferential strain profiles, end bearing, and shaft friction mobilization under static monotonic loading which contributed to the design of pile foundation. The main findings are as follows:

(a) The novel distributed sensing technique of distributed (OFDR) optic sensors is able to monitor the axial strain profiles along the FRP composite SSC piles, demonstrating good agreement with one another and with LVDT calculated strain data. The OFDR sensors monitor the distributed strain profiles with high spatial resolution providing load distribution of the entire pile, identifying any localized regions of weakness, strain concentrations, or pile shaft non-homogeneity with higher accuracy and hence overcoming the limitations of traditional monitoring techniques.

(b) The axial strain profiles measured by different fibers at different positions of the cross-section along the depth of the piles showed a similar trend for both model piles with higher localized strain values recorded in the upper one-third region near the pile head. This localized strain concentration led to failure of both piles in the form of cracks and rebars crushing in both piles during the failure stage.

(c) The axial strain profiles within rock-socket were utilized to develop load transfer curves to calculate reliable shaft friction values that may be used in future pile design of similar conditions. The maximum shaft friction was mobilized in the upper one-third region of the socket.

(d) The mean shaft friction mobilized early at smaller displacement with maximum up to 3.3 MPa and 4 MPa compared to end bearing pressure which mobilized at higher displacement with maximum up to 4.85 MPa and 5.5MPa for Pile I and II respectively. The observed shaft friction values between the rock and pile shaft were higher compared to conventional designs showing underestimation of actual values.

(e) The distributed circumferential strain profiles provided reliable information of the localized strain concentrations around the pile circumference, showing early detection of pile shaft cracks, lateral deformation, and bending direction and position accurately.

(f) The predicted buckling load based on analytical solutions and actual buckling load from tests were in fair agreement with a minor discrepancy due to localized strains near the pile head.

In conclusion, the physical model tests of FRP composite SSC piles using a novel distributed sensing technique provided detailed information on both the axial and radial strain profiles that could be used for early design assumptions of piles in the field and for the potential predictive tools. In future comparative studies, LVDTs will be instrumented at the rock surface, which may provide the pile base settlement more accurately and its comparison with pile body deformation above rock surface may offer better justification for validating fiber optic sensors and LVDTs results.

Data Availability Statement

Some or all data, models, or code that support the findings of this study are available from the corresponding author upon reasonable request.

Acknowledgments

The above research was funded by a Theme-based Research Scheme project (T22-502/18-R), a Research Impact Fund project (R5037-18) and GRF projects (15210020, 15210322, 15226722, and 15231122) from the Research Grants Council of Hong Kong Special Administrative Region Government of China, respectively. The authors of this work also gratefully acknowledged the financial support provided by PolyU (BD8U), the Research Institute of Land and Space (CD82, CD7A), and Research Centre for Resources Engineering towards Carbon Neutrality of PolyU (BBEJ).

References

Bersan, S., Bergamo, O., Palmieri, L., Schenato, L., and Simonini, P. (2018). Distributed strain measurements in a CFA pile using high spatial resolution fibre optic sensors. *Engineering Structures*, *160*, 554-565.

Carter, J., and Kulhawy, F. H. (1988). *Analysis and design of drilled shaft foundations socketed into rock* (No. EPRI-EL-5918). Electric Power Research Inst., Palo Alto, CA (USA); Cornell Univ., Ithaca, NY (USA). Geotechnial Engineering Group.

Chen, Z., Chen, W.-B., Yin, J.-H., and Malik, N. (2021). Shaft Friction Characteristics of Two FRP Seawater Sea–Sand Concrete Piles in a Rock Socket with or without Debris. *International Journal of Geomechanics*, *21*(7), 06021015.

Code, C.-F. M. (1990). CEB-FIP model code for concrete structures, euro-international committe for concrete. *Bulletin*(213/214).

Davisson, M., and Robinson, K. (1965). Bending and buckling of partially embedded piles. *Soil Mech & Fdn Eng Conf Proc/Canada/*.

Fam, A., Flisak, B., and Rizkalla, S. (2003). Experimental and analytical modeling of concrete-filled FRP tubes subjected to combined bending and axial loads. *ACI Struct. J*, *100*(4), 499-509.

Gill, S. A. (1980). Design and construction of rock caissons. In *International Conference on Structural Foundations on Rock, 1980, Sydney, Australia* (Vol. 1).

Hauswirth, D., Puzrin, A. M., Carrera, A., Standing, J. R., and Wan, M. S. P. (2014). Use of fibre-optic sensors for simple assessment of ground surface displacements during tunnelling. *Géotechnique*, *64*(10), 837-842. https://doi.org/10.1680/geot.14.T.009

Heelis, M., Pavlović, M., and West, R. (2004). The analytical prediction of the buckling loads of fully and partially embedded piles. *Géotechnique*, *54*(6), 363-373.

Hetényi, M., and Hetbenyi, M. I. (1946). *Beams on elastic foundation: theory with applications in the fields of civil and mechanical engineering* (Vol. 16). University of Michigan press Ann Arbor, MI.

Hong, C.-Y., Zhang, Y.-F., and Liu, L.-Q. (2016). Application of distributed optical fiber sensor for monitoring the mechanical performance of a driven pile. *Measurement*, *88*, 186-193.

Horvath, R. G., and Kenney, T. C. (1979). Shaft resistance of rock-socketed drilled piers. In *Symposium on Deep Foundations* (pp. 182-214). ASCE.

Iten, M., Puzrin, A. M., and Schmid, A. (2008). Landslide monitoring using a road-embedded optical fiber sensor. *Smart Sensor Phenomena, Technology, Networks, and Systems* 2008.

Kaderabek, T. J., and Reynolds, R. T. (1981). Miami limestone foundation design and construction. *Journal of the Geotechnical Engineering Division*, *107*(7), 859-872.

Krauss, P. D., and Nmai, C. K. (1996). Preliminary corrosion investigation of prestressed concrete piles in a marine environment: Deerfield beach fishing pier. *ASTM special technical publication*, *1276*, 161-172.

Lee, J. S., and Park, Y. H. (2008). Equivalent pile load–head settlement curve using a bi-directional pile load test. *Computers and Geotechnics*, *35*(2), 124-133.

Li, H.-N., Li, D.-S., and Song, G.-B. (2004). Recent applications of fiber optic sensors to health monitoring in civil engineering. *Engineering Structures*, *26*(11), 1647-1657.

Li, H. N., Zhou, G. D., Ren, L., & Li, D. S. (2009). Strain transfer coefficient analyses for embedded fiber Bragg grating sensors in different host materials. Journal of engineering mechanics, 135(12), 1343-1353.

Lin, S. Q., Tan, D. Y., Yin, J. H., and Li, H. (2021). A Novel Approach to Surface Strain Measurement for Cylindrical Rock Specimens Under Uniaxial Compression Using Distributed Fibre Optic Sensor Technology. *Rock Mechanics and Rock Engineering*, *54*(12), 6605-6619.

Lin, S. Q., Tan, D.Y., Yin, Leung Y.F, Yin J. H., Li, I. Sze, E.H.Y., Lo, F. L. C., Kan, H.S., Wong,T. C. W., and Chan, E. Y.M. (2023). Fibe-optic monitoring of a twin circular shaft excavation: development of circumferential forces and bending moments in a diaphragm wall. *Journal of Geotechnical and GeoenvironmentalEngineering*,DOI:10.106/JGGEFK.GTEN-11211.

Lin, S. (2023). Refined monitoring using the OFDR-based distributed fibre optic sensor: from laboratory tests to site monitoring. PhD thesis, The Hong Kong Polytechnic University

Mandolini, A., Russo, G., and Viggiani, C. (2005). Pile foundations: Experimental investigations, analysis and design. In *Proceedings of the international conference on soil mechanics and geotechnical engineering* (Vol. 16, No. 1, p. 177). AA Balkema Publishers.

Mirmiran, A., Shahawy, M., and Samaan, M. (1999). Strength and ductility of hybrid FRP-concrete beam-columns. *Journal of structural engineering*, *125*(10), 1085-1093.

Mohamad, H., Bennett, P. J., Soga, K., Mair, R. J., & Bowers, K. (2010). Behaviour of an old masonry tunnel due to tunnelling-induced ground settlement. *Géotechnique*, 60(12), 927-938.

Ng, C. W., Yau, T. L., Li, J. H., and Tang, W. H. (2001). Side resistance of large diameter bored piles socketed into decomposed rocks. *Journal of Geotechnical and Geoenvironmental Engineering*, *127*(8), 642-657.

O'Neill, M., Townsend, F., Hassan, K., Buller, A., and Chan, P. (1996). *Load transfer for drilled shafts in intermediate geomaterials* (No. FHWA-RD-95-172). United States. Department of Transportation. Federal Highway Administration.

Pando, M. A., Ealy, C. D., Filz, G. M., Lesko, J., and Hoppe, E. (2006). *A laboratory and field study of composite piles for bridge substructures* (No. FHWA-HRT-04-043). United States. Federal Highway Administration. Office of Infrastructure Research and Development.

Park, J.-H., Jo, B.-W., Yoon, S.-J., and Park, S.-K. (2011). Experimental investigation on the structural behavior of concrete filled FRP tubes with/without steel re-bar. *KSCE Journal of Civil Engineering*, *15*(2), 337-345.

Pei, H. F., Teng, J., Yin, J. H., and Chen, R. (2014). A review of previous studies on the applications of optical fiber sensors in geotechnical health monitoring. *Measurement*, *58*, 207-214.

Pelecanos, L., Soga, K., Elshafie, M. Z., de Battista, N., Kechavarzi, C., Gue, C. Y., Ouyang, Y., and Seo, H.-J. (2018). Distributed fiber optic sensing of axially loaded bored piles. *Journal of Geotechnical and Geoenvironmental Engineering*, *144*(3), 04017122.

Prakash, S. (1987). Buckling loads of fully embedded vertical piles. *Computers and Geotechnics*, *4*(2), 61-83.

O'Neil, M. W., and Reese, L. C. (1999). *Drilled shafts: Construction procedures and design methods* (No. FHWA-IF-99-025). United States. Federal Highway Administration. Office of Infrastructure.

Rosenberg, P., and Journeaux, N. L. (1976). Friction and end bearing tests on bedrock for high capacity socket design. *Canadian Geotechnical Journal*, *13*(3), 324-333.

Rowe, R., and Armitage, H. (1987). A design method for drilled piers in soft rock. *Canadian Geotechnical Journal*, *24*(1), 126-142.

Sakr, M., Naggar, M. H. E., and Nehdi, M. (2004). Novel toe driving for thin-walled piles and performance of fiberglass-reinforced polymer (FRP) pile segments. *Canadian Geotechnical Journal*, *41*(2), 313-325.

Schenato, L. (2017). A review of distributed fibre optic sensors for geo-hydrological applications. *Applied Sciences*, *7*(9), 896.

Seidel, J., and Collingwood, B. (2001). A new socket roughness factor for prediction of rock socket shaft resistance. *Canadian Geotechnical Journal*, *38*(1), 138-153.

Soga, K. (2014). Understanding the real performance of geotechnical structures using an innovative fibre optic distributed strain measurement technology. *Riv. Ital. Geotech*, *4*, 7-48.

Toh, C., Ooi, T., Chiu, H., Chee, S., and Ting, W. (1989). Design parameters for bored piles in a weathered sedimentary formation. Congrès international de mécanique des sols et des travaux de fondations. 12,

Williams, A., and Pells, P. (1981). Side resistance rock sockets in sandstone, mudstone, and shale. *Canadian Geotechnical Journal*, *18*(4), 502-513.

Wu, J., Liu, H., Yang, P., Tang, B., & Wei, G. (2020). Quantitative strain measurement and crack opening estimate in concrete structures based on OFDR technology. *Optical Fiber Technology*, 60, 102354.

Wu, P.-C., Chen, W.-B., Yin, J.-H., Pan, Y., Lou, K., and Feng, W.-Q. (2022). A Novel Sensor for Undrained Shear Strength Measurement in Very Soft to Soft Marine Sediments Based on Optical Frequency Domain Reflectometry Technology. *Sensors*, *22*(15), 5530.

Wu, P.-C., Tan, D.-Y., Chen, W.-B., Malik, N., and Yin, J.-H. (2021). Novel fiber Bragg Grating-based strain gauges for monitoring dynamic responses of Celtis sinensis under typhoon conditions. *Measurement*, *172*, 108966.

Wu, P., Tan, D., Lin, S., Chen, W., Yin, J., Malik, N., and Li, A. (2022). Development of a monitoring and warning system based on optical fiber sensing technology for masonry retaining walls and trees. *Journal of Rock Mechanics and Geotechnical Engineering*, *14*(4), 1064-1076.

Xiao, J., Qiang, C., Nanni, A., and Zhang, K. (2017). Use of sea-sand and seawater in concrete construction: Current status and future opportunities. *Construction and Building Materials*, *155*, 1101-1111.

Zhan, C., and Yin, J.-H. (2000). Field static load tests on drilled shaft founded on or socketed into rock. *Canadian Geotechnical Journal*, *37*(6), 1283-1294.

Zhang, D., Shi, B., Sun, Y., Tong, H., and Wang, G. (2015). Bank slope monitoring with integrated fiber optical sensing technology in Three Gorges Reservoir Area. In *Engineering Geology for Society and Territory-Volume 2: Landslide Processes* (pp. 135-138). Springer International Publishing. Zheng, X., Shi, B., Zhu, H.-H., Zhang, C.-C., Wang, X., and Sun, M.-Y. (2021). Performance monitoring of offshore PHC pipe pile using BOFDA-based distributed fiber optic sensing system. *Geomechanics and Engineering*, *24*(4), 337-348.

Zhang, Q., Sun, Y., Zhang, Z., Zeng, P., Duan, J., Zhu, N., ... & Rong, F. (2019). Strain transfer in distributed fiber optic sensor with optical frequency domain reflectometry technology. *Optical Engineering*, 58(2), 027109-027109.

Zyka, K., and Mohajerani, A. (2016). Composite piles: A review. *Construction and Building Materials*, *107*, 394-410.

Figure captions

Fig. 1. OFDR sensing principle

Fig. 2. FBG sensing principle

Fig. 3. Setup of the whole physical model system

Fig. 4. Cross-section illustrations of Pile I: (a) vertical profile, (b) horizontal profile

Fig. 5. Cross-section illustrations of Pile II: (a) vertical profile, (b) horizontal profile

Fig. 6. (a) Axial strain distribution of Pile I measured from OFDR and FBGs, and (b) overall integrated axial strain from measured results from OFDR and FBGs versus the overall strain results from LVDT

Fig. 7. Axial strain distribution of Pile I under different loading levels monitored with different OFDR fiber sections: (a) S1, (b) S4, (c) S5, (d) S6, and (e) strain profile of different fiber sections under peak load of 213 kN

Fig. 8. Socket response of Pile I: (a) shaft friction profiles calculated from different OFDR fiber sections data under different loading levels, (b) mean shaft friction and end bearing pressure against applied load, and (c) shaft and base resistance against displacement

Fig. 9. Circumferential strain distribution of Pile I monitored under different loading levels with different OFDR optic fibers sections: (a) S8, (b) S9, (c) S12, and (d) S14

Fig. 10. Comparison of axial and circumferential strain profiles of Pile I with final failure shape and buckling mode

Fig. 11. (a) Axial strain distribution of Pile II measured from OFDR and FBGs, and (b) overall integrated axial strain from measured results from OFDR and FBGs versus the overall strain results from LVDT

Fig. 12. Axial strain distribution of Pile II monitored with different OFDR fiber sections under different loading levels: (a) S1, (b) S9, (c) S11, (d) S12, and (e) strain profile of different fiber sections under peak load of 266 kN

Fig. 13. Socket response of Pile II: (a) shaft friction profiles calculated from different OFDR fiber sections data under different loading levels, (b) mean shaft friction and end bearing pressure against applied load, and (b) shaft and base resistance against displacement

Fig. 14. Circumferential strain distribution of Pile II monitored at different under different loading levels with different OFDR optic fiber sections: (a) S8, (b) S7, (c) S5, and (d) S2

Fig. 15. Comparison of axial and circumferential strain profiles of Pile II with final failure shape and buckling mode

Fig. 16. Partially embedded pile system: (a) actual pile, and (b) equivalent system based on (after Heelis et al., 2004)

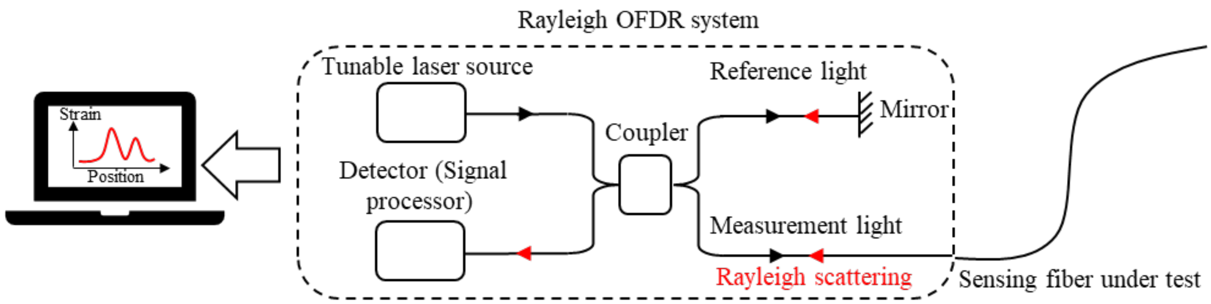

Fig. 1. OFDR sensing principle

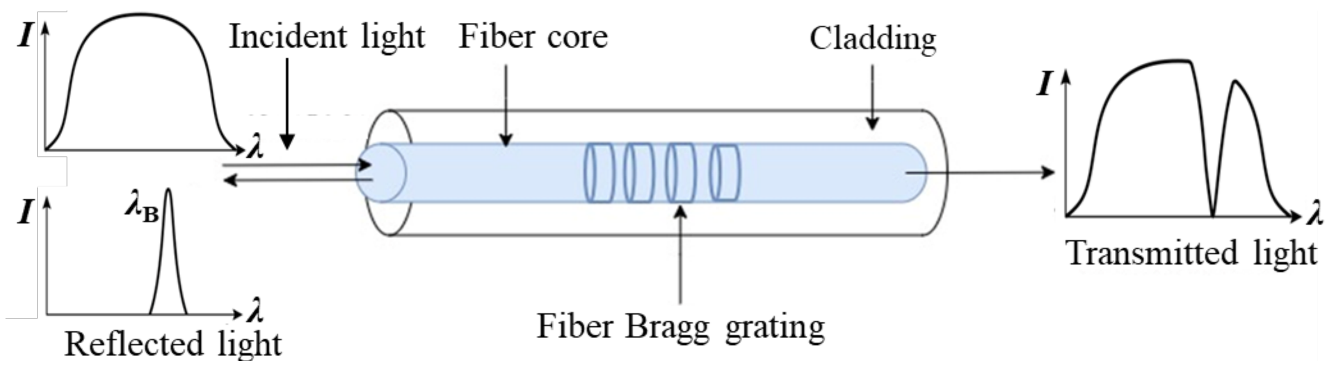

Fig. 2. FBG sensing principle

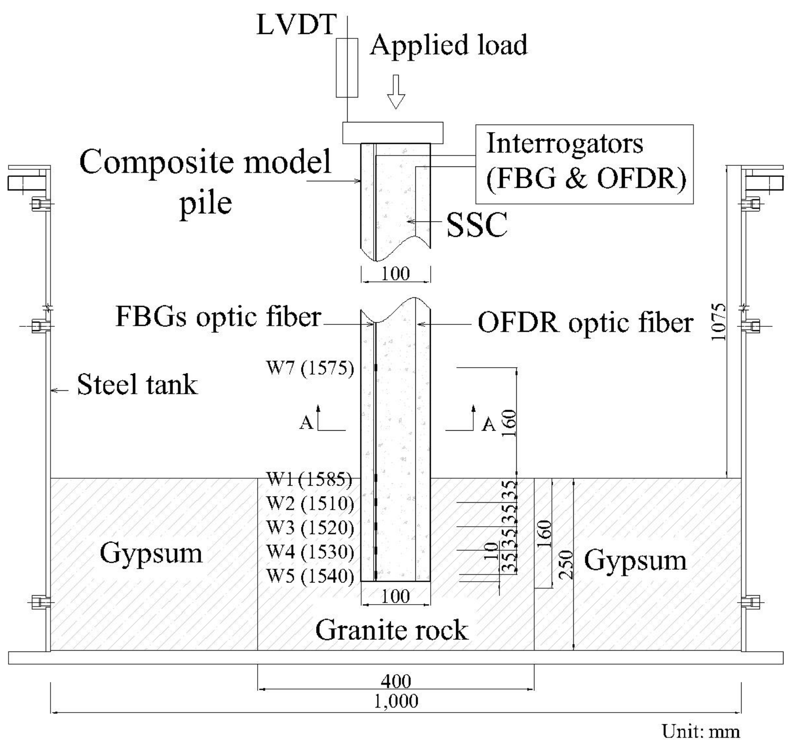

Fig. 3. Setup of the whole physical model system

841 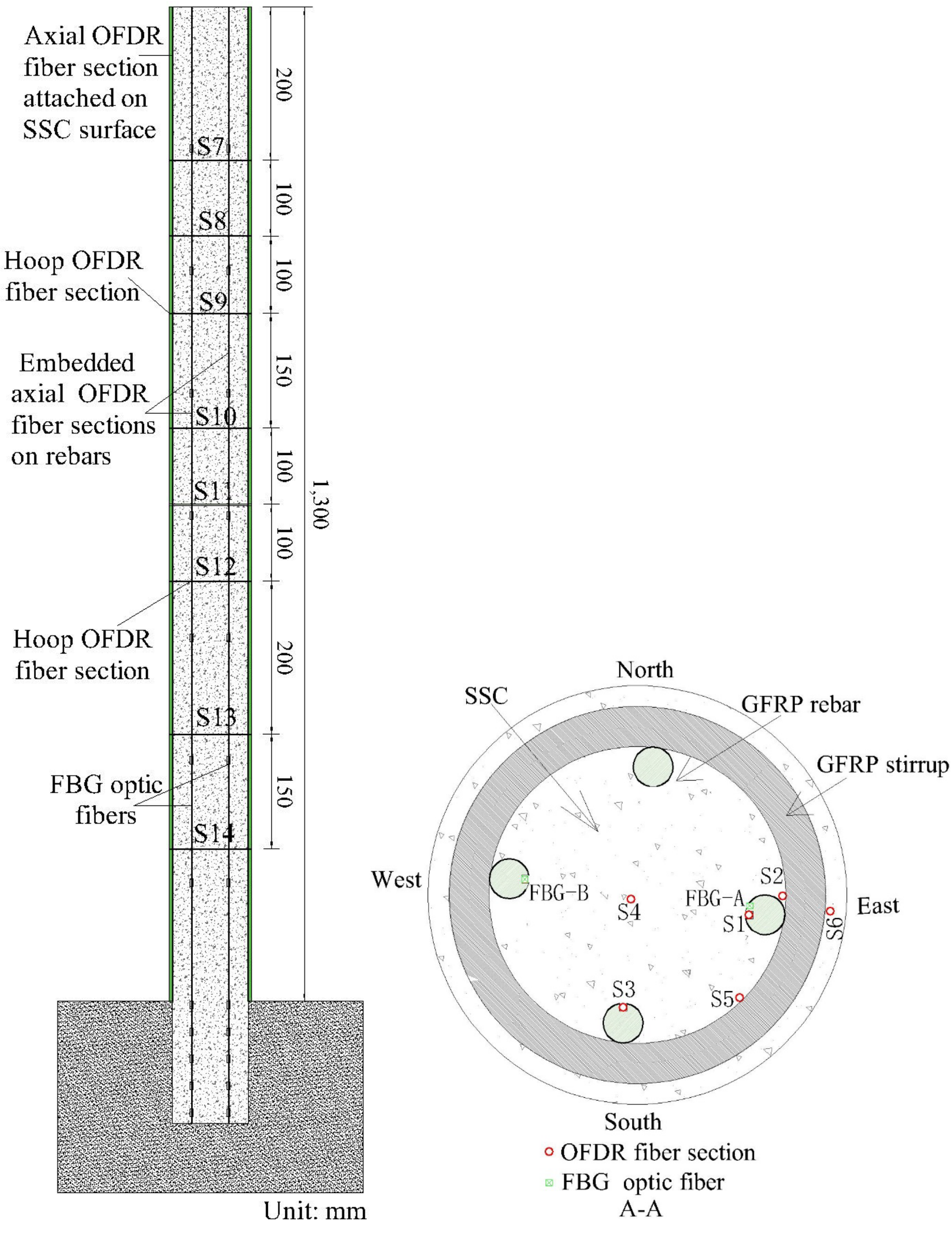

(a) (b)

842 **Fig. 4.** Cross-section illustrations of Pile I: (a) vertical profile, (b) horizontal profile

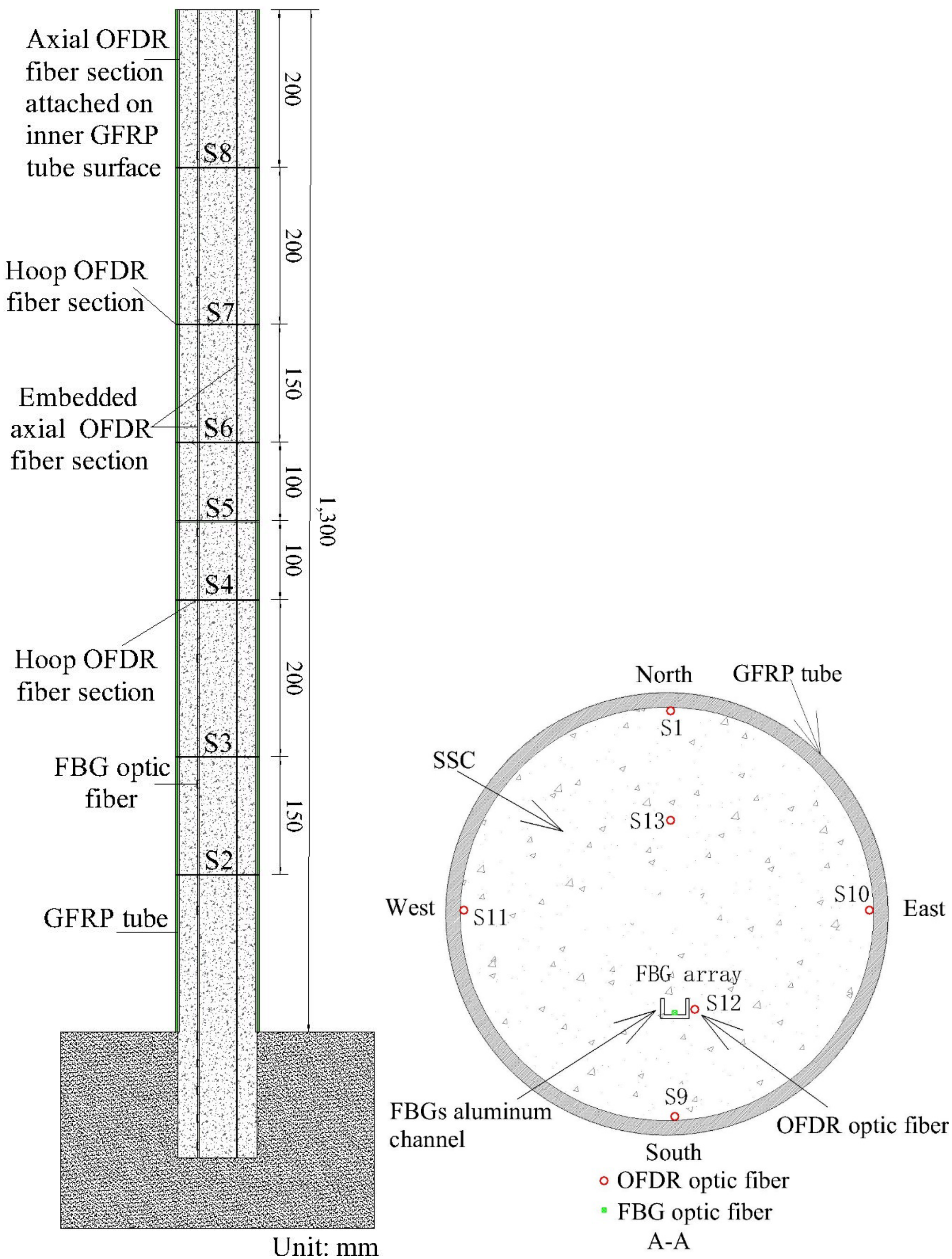

(a) (b)

Fig. 5. Cross-section illustrations of Pile II: (a) vertical profile, (b) horizontal profile

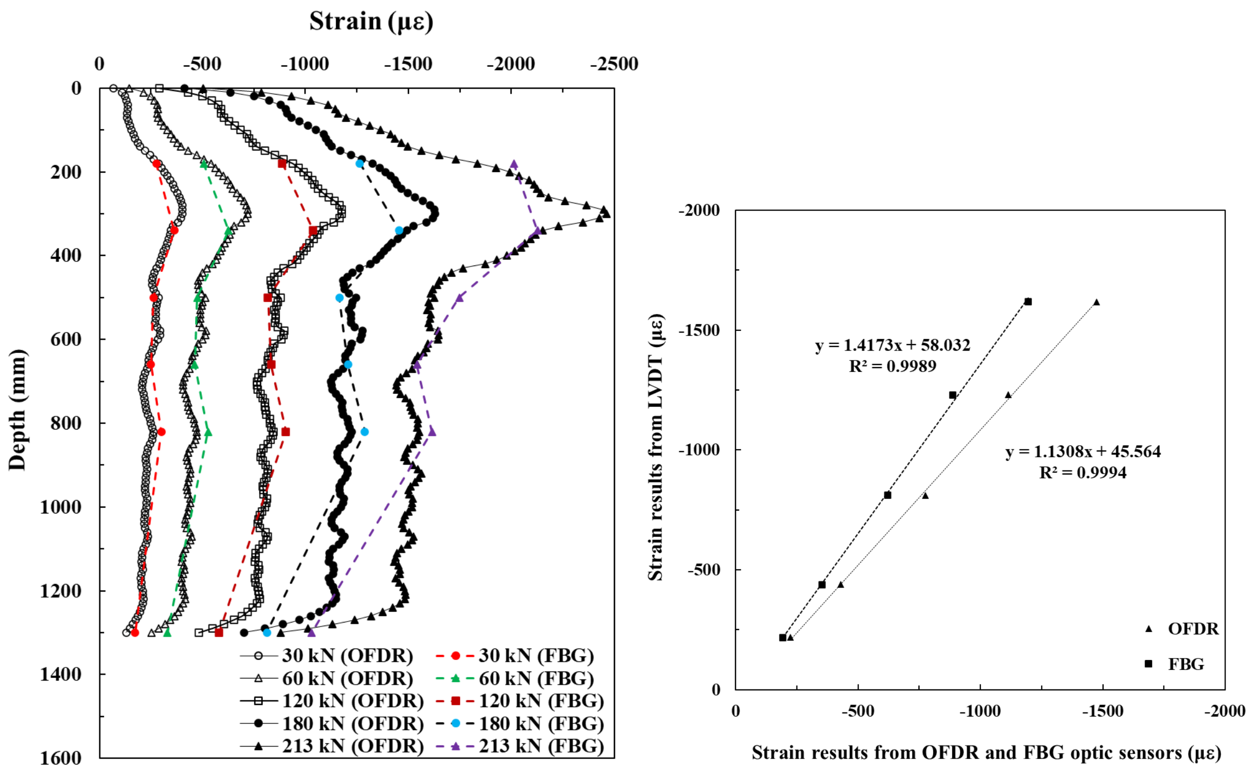

(a) (b)

Fig. 6. (a) Axial strain distribution of Pile I measured from OFDR and FBGs, and (b) overall integrated axial strain from measured results from OFDR and FBGs versus the overall strain results from LVDT

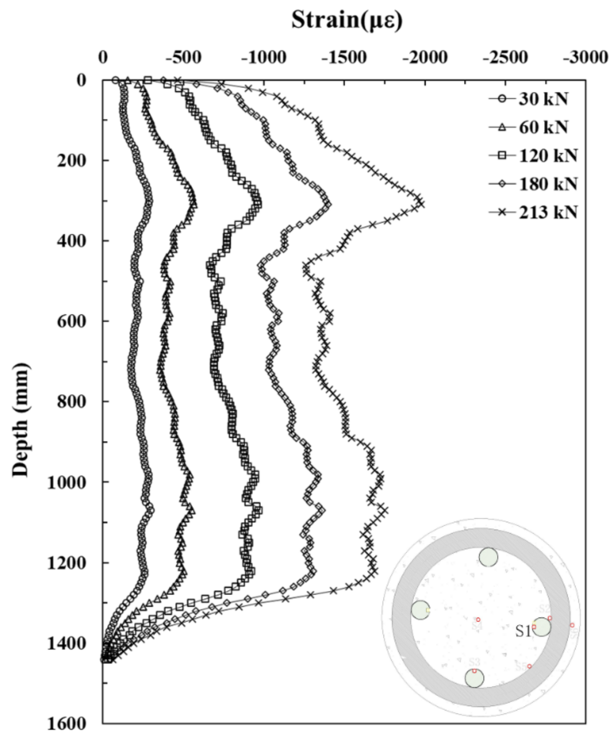
Strain(με)
0
-500
-1000
-1500
-2000
-2500
-3000
Depth (mm)
0
200
400
600
800
1000
1200
1400
1600
30 kN
60 kN
120 kN
180 kN
213 kN
S1

(a)

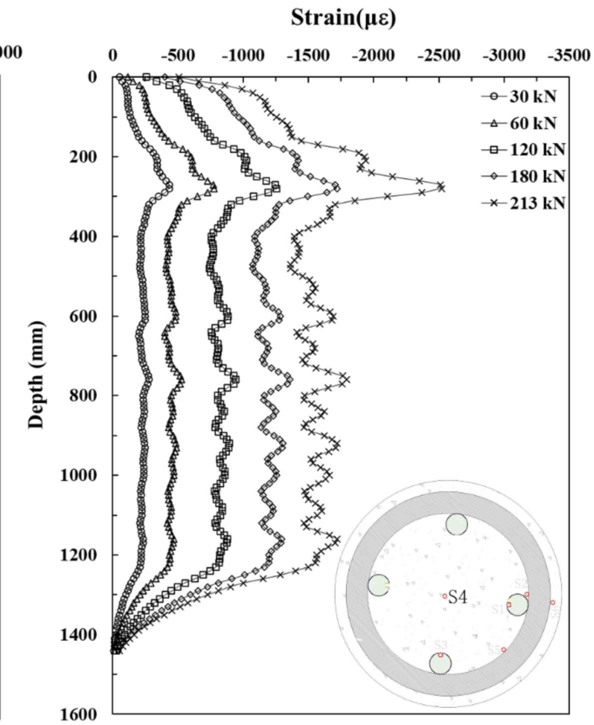
Strain(με)
0
-500
-1000
-1500
-2000
-2500
-3000
-3500
Depth (mm)
0
200
400
600
800
1000
1200
1400
1600
30 kN
60 kN
120 kN
180 kN
213 kN
S4

(b)

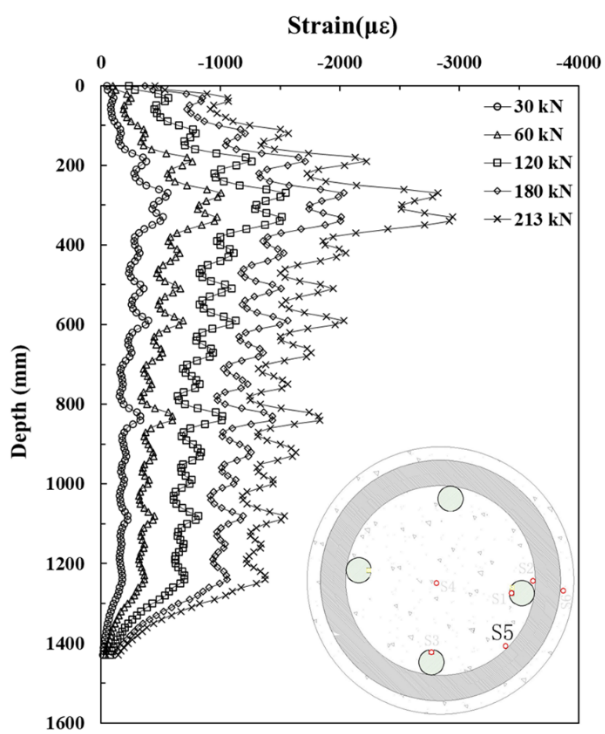
Strain(με)
0
-1000
-2000
-3000
-4000
Depth (mm)
0
200
400
600
800
1000
1200
1400
1600
30 kN
60 kN
120 kN
180 kN
213 kN
S5

(c)

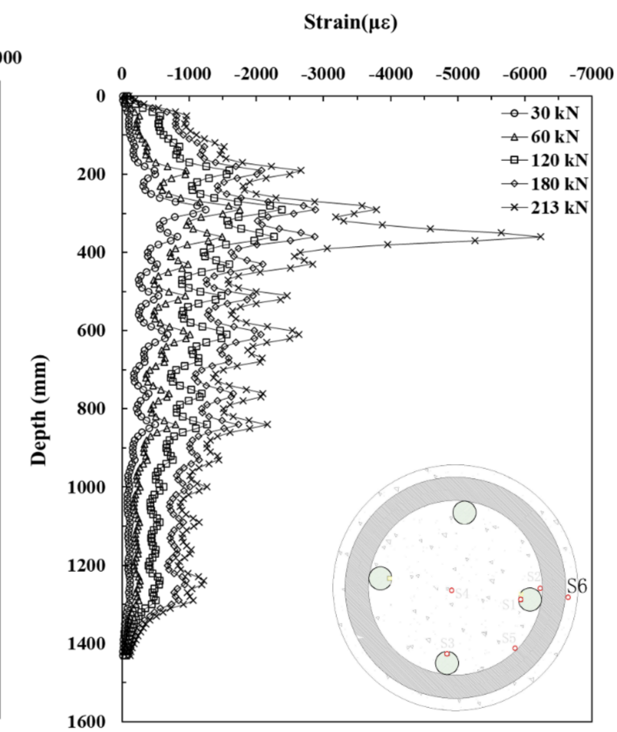
Strain(με)
0
-1000
-2000
-3000
-4000
-5000
-6000
-7000
Depth (mm)
0
200
400
600
800
1000
1200
1400
1600
30 kN
60 kN
120 kN
180 kN
213 kN
S6

(d)

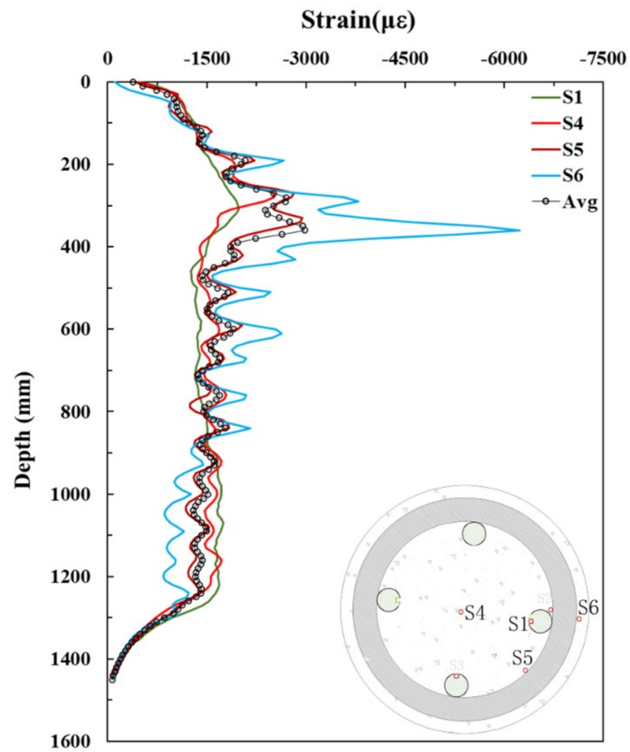

(e)

Fig. 7. Axial strain distribution of Pile I under different loading levels monitored with different OFDR fiber sections: (a) S1, (b) S4, (c) S5, (d) S6, and (e) strain profile of different fiber sections under peak load of 213 kN

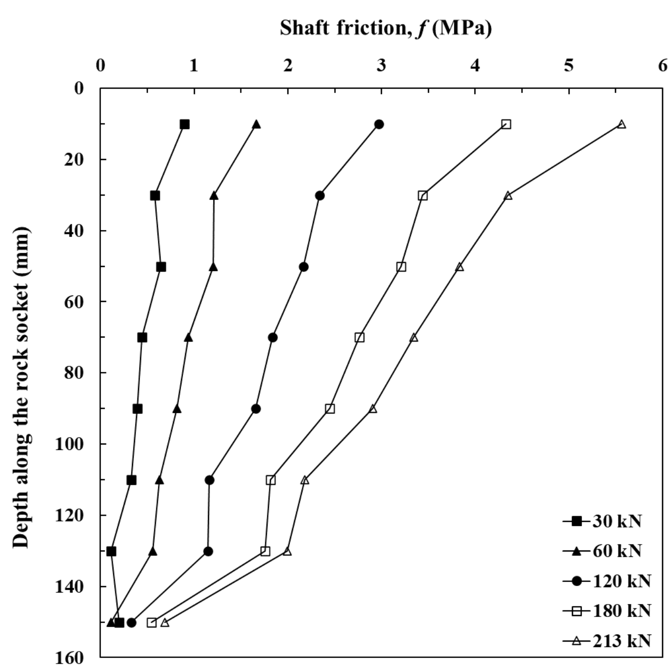

(a)

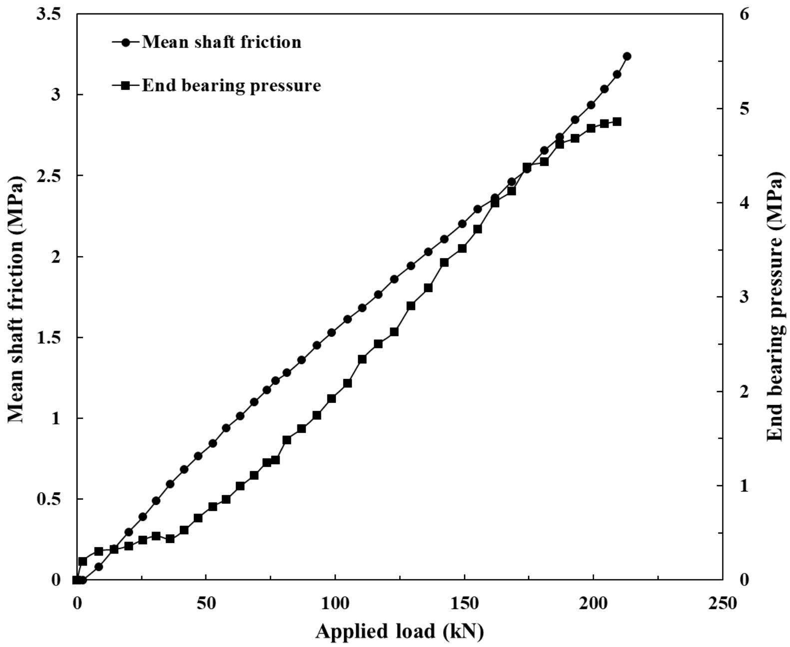
Mean shaft friction
End bearing pressure
Mean shaft friction (MPa)
End bearing pressure (MPa)
Applied load (kN)
0
0.5
1
1.5
2
2.5
3
3.5
0
1
2
3
4
5
6
0
50
100
150
200
250

(b)

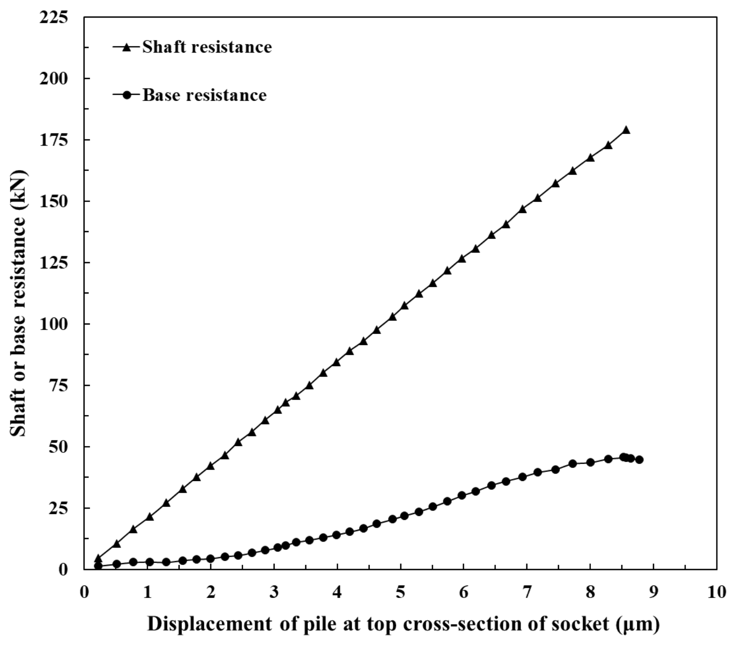
Shaft resistance
Base resistance
Shaft or base resistance (kN)
Displacement of pile at top cross-section of socket (μm)
0
25
50
75
100
125
150
175
200
225
0
1
2
3
4
5
6
7
8
9
10

(c)

Fig. 8. Socket response of Pile I: (a) shaft friction profiles calculated from different OFDR fiber sections data under different loading levels, (b) mean shaft friction and end bearing pressure against applied load, and (c) shaft and base resistance against displacement

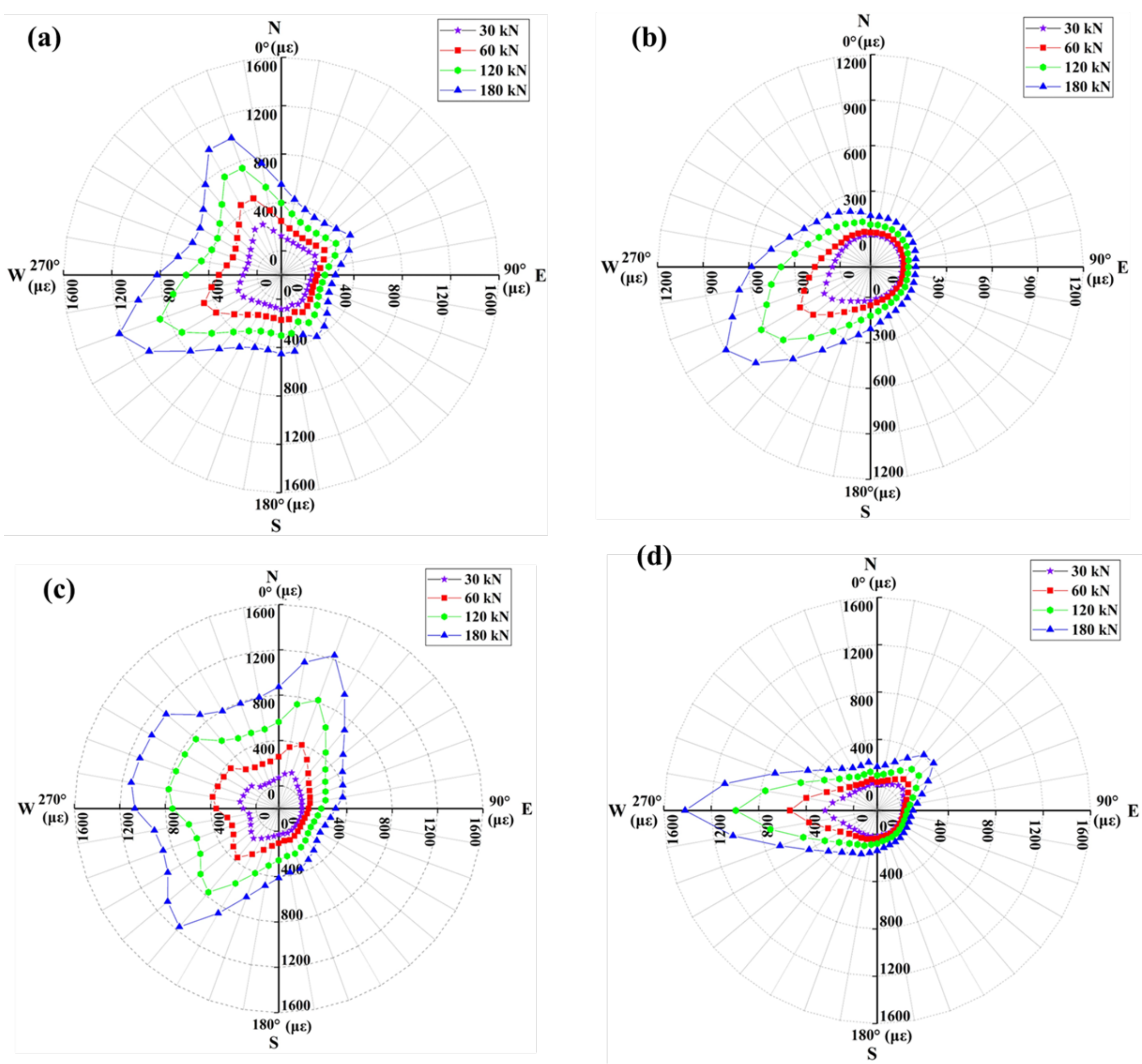

Fig. 9. Circumferential strain distribution of Pile I monitored under different loading levels with different OFDR optic fibers sections: (a) S8, (b) S9, (c) S12, and (d) S14

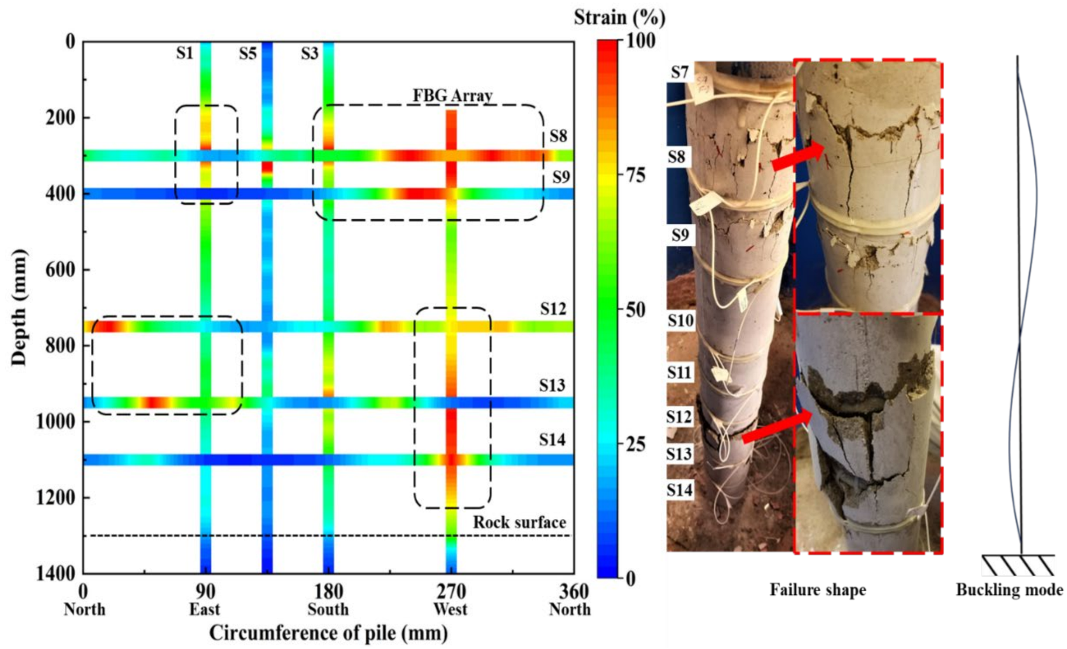

Fig. 10. Comparison of axial and circumferential strain profiles of Pile I with final failure shape and buckling mode

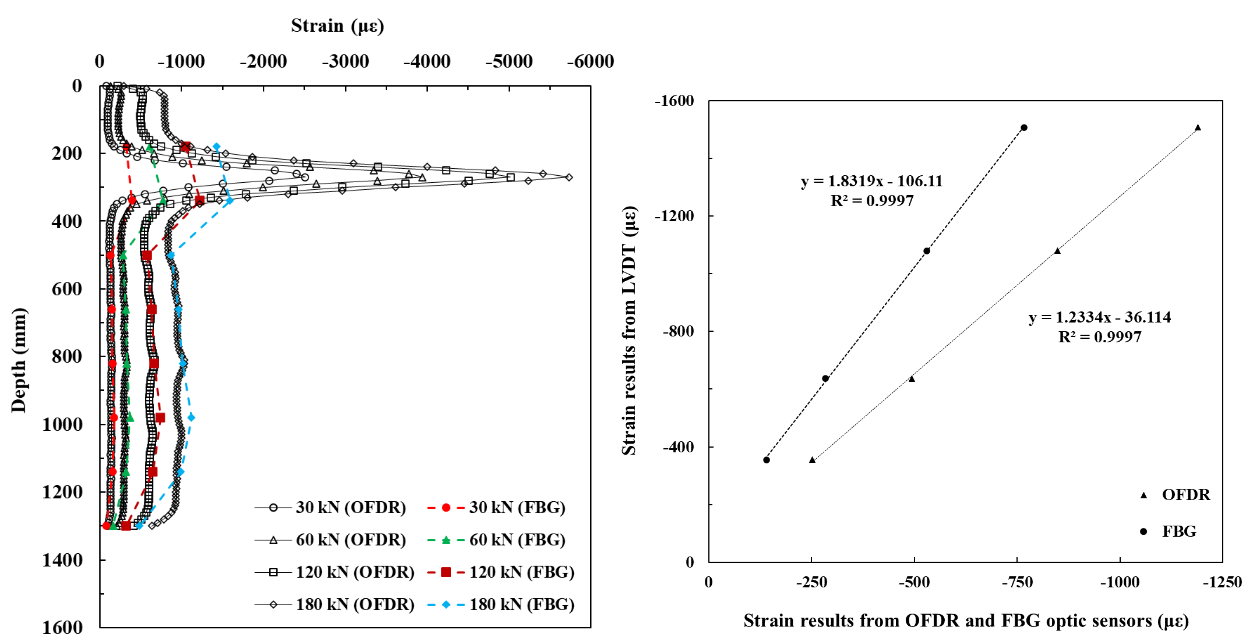

(a) (b)

Fig. 11. (a) Axial strain distribution of Pile II measured from OFDR and FBGs, and (b) overall integrated axial strain from measured results from OFDR and FBGs versus the overall strain results from LVDT

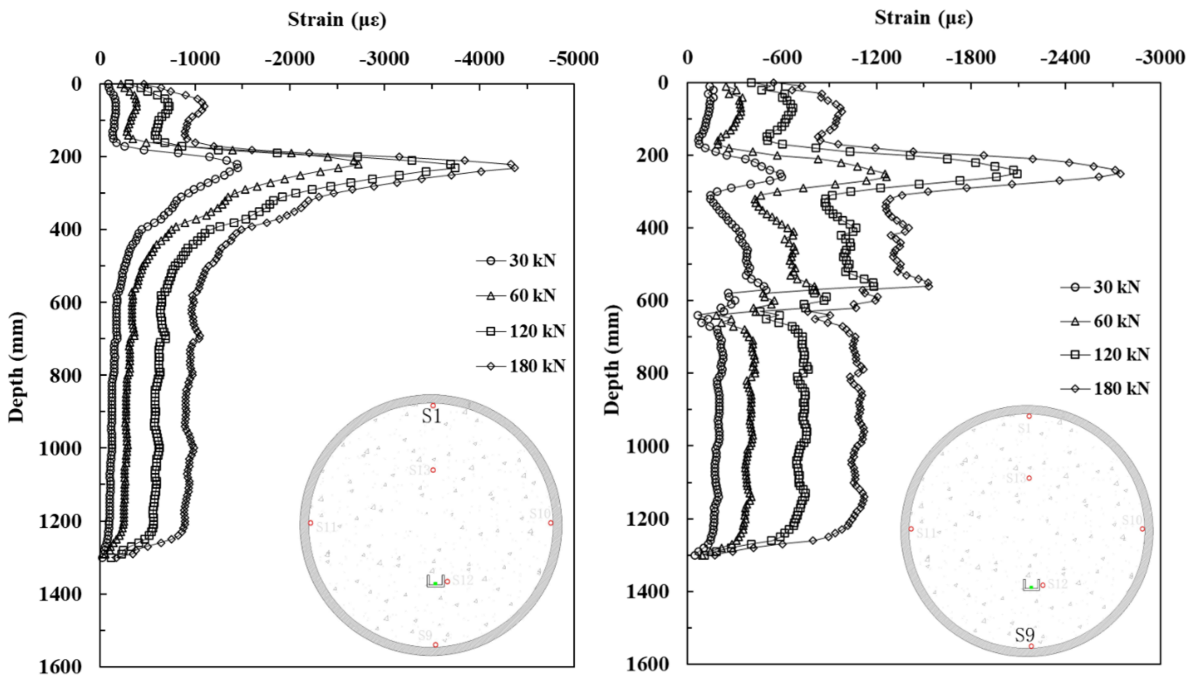

(a) (b)

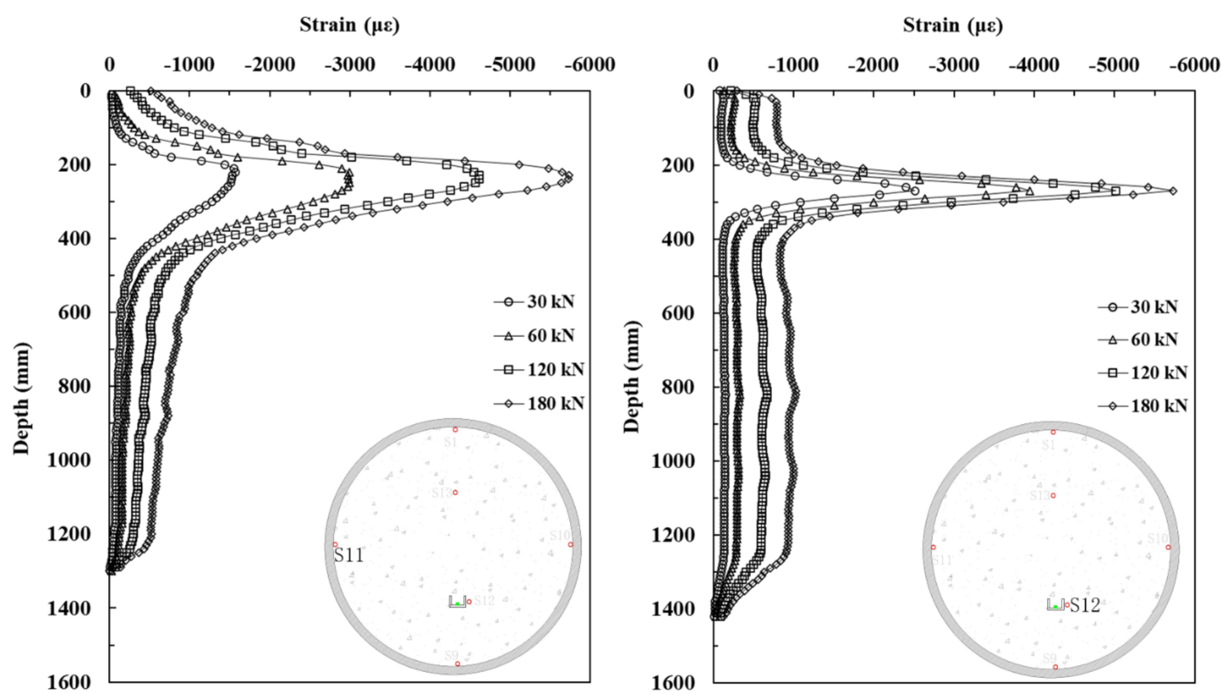

(c) (d)

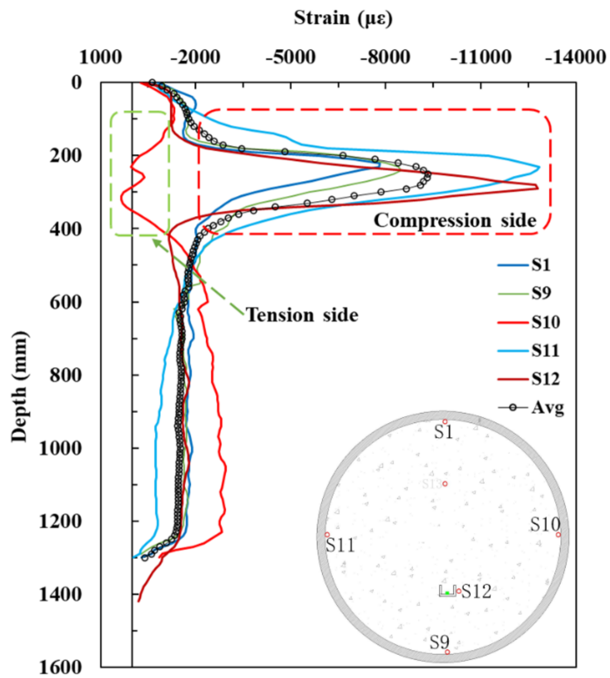

(e)

Fig. 12. Axial strain distribution of Pile II monitored with different OFDR fiber sections under different loading levels: (a) S1, (b) S9, (c) S11, (d) S12, and (e) strain profile of different fiber sections under peak load of 266 kN

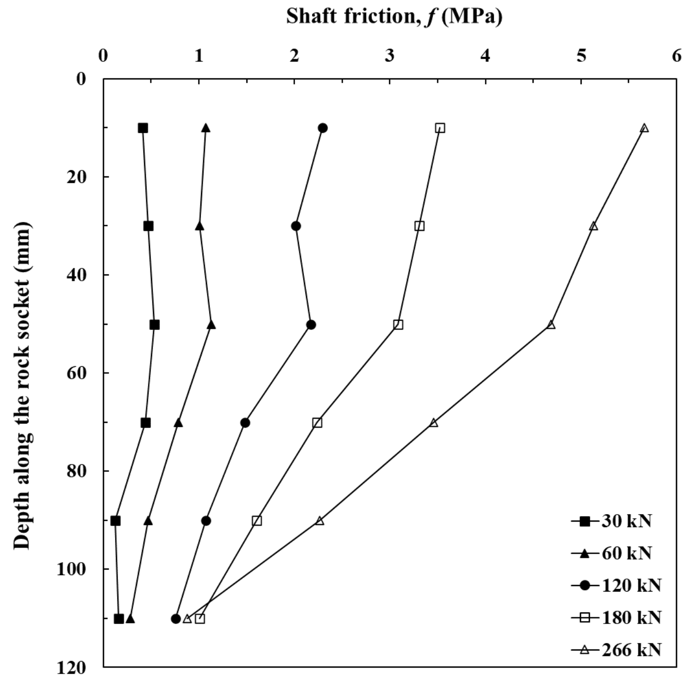
Shaft friction, f (MPa)
0
1
2
3
4
5
6
Depth along the rock socket (mm)
0
20
40
60
80
100
120
30 kN
60 kN
120 kN
180 kN
266 kN

(a)

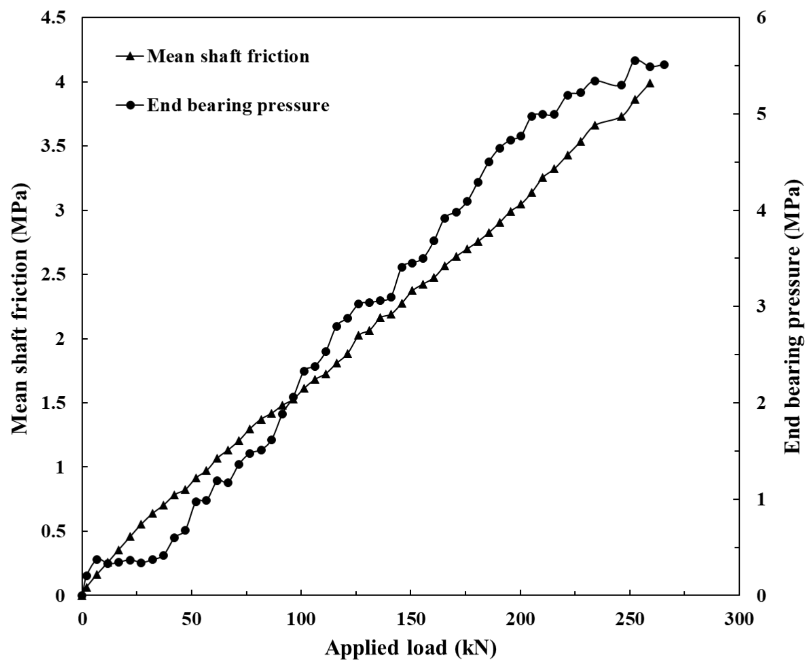
Mean shaft friction
End bearing pressure
Mean shaft friction (MPa)
0
0.5
1
1.5
2
2.5
3
3.5
4
4.5
End bearing pressure (MPa)
0
1
2
3
4
5
6
Applied load (kN)
0
50
100
150
200
250
300

(b)

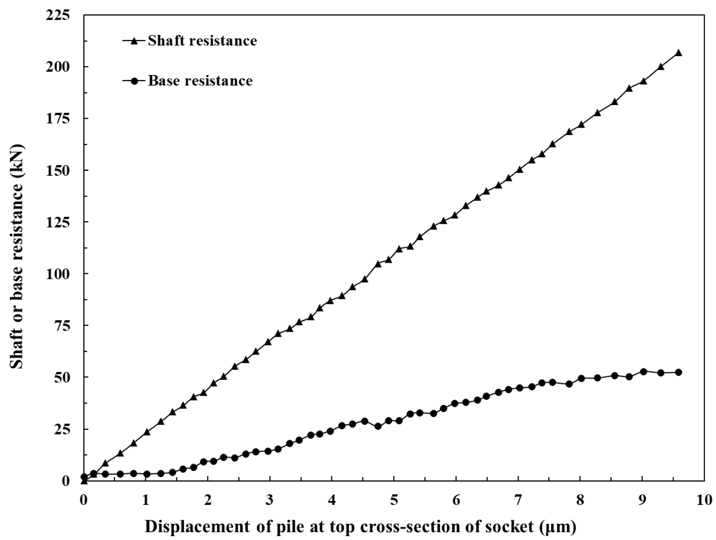

(c)

Fig. 13. Socket response of Pile II: (a) shaft friction profiles calculated from different OFDR fiber sections data under different loading levels, (b) mean shaft friction and end bearing pressure against applied load, and (b) shaft and base resistance against displacement

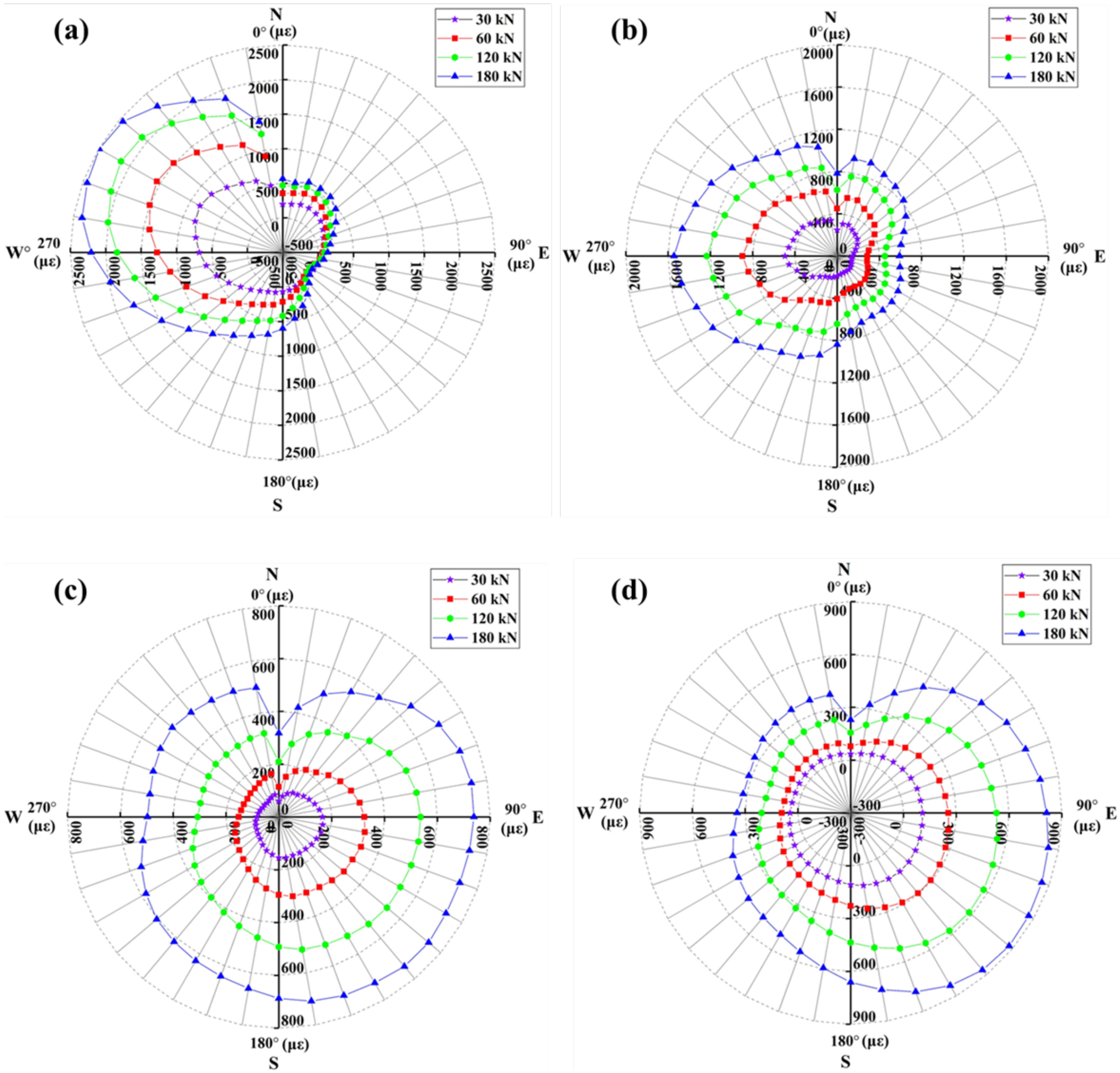

Fig. 14. Circumferential strain distribution of Pile II monitored at different under different loading levels with different OFDR optic fiber sections: (a) S8, (b) S7, (c) S5, and (d) S2

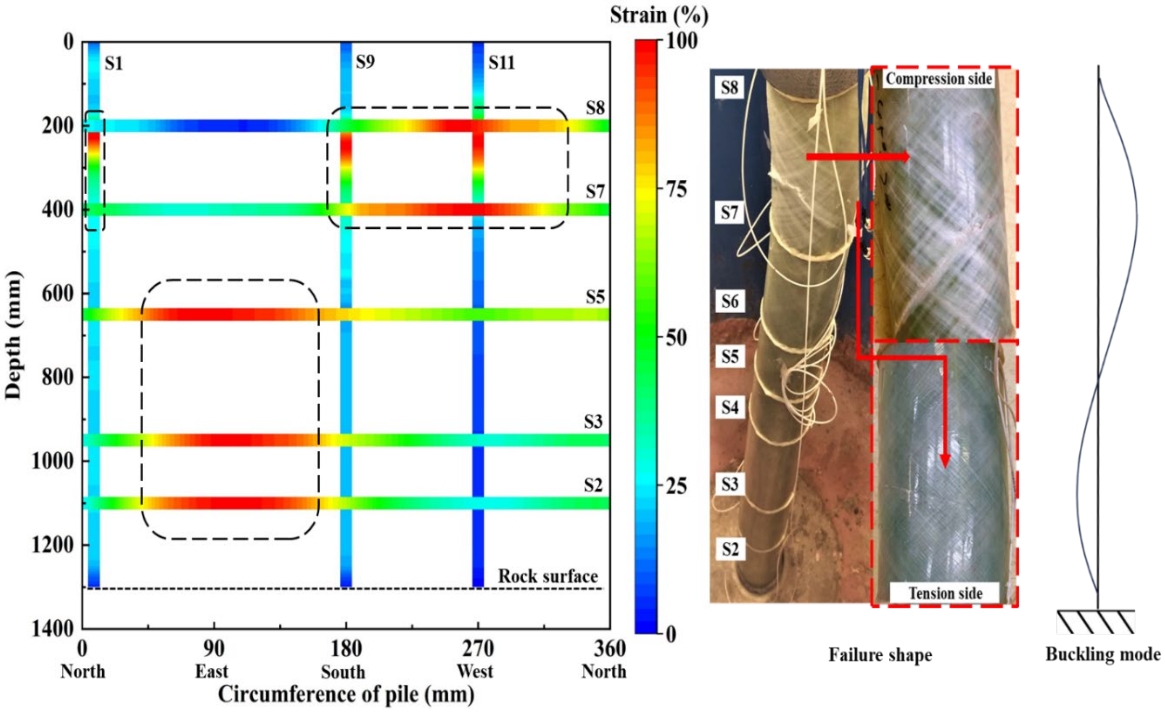

Fig. 15. Comparison of axial and circumferential strain profiles of Pile II with final failure shape and buckling mode

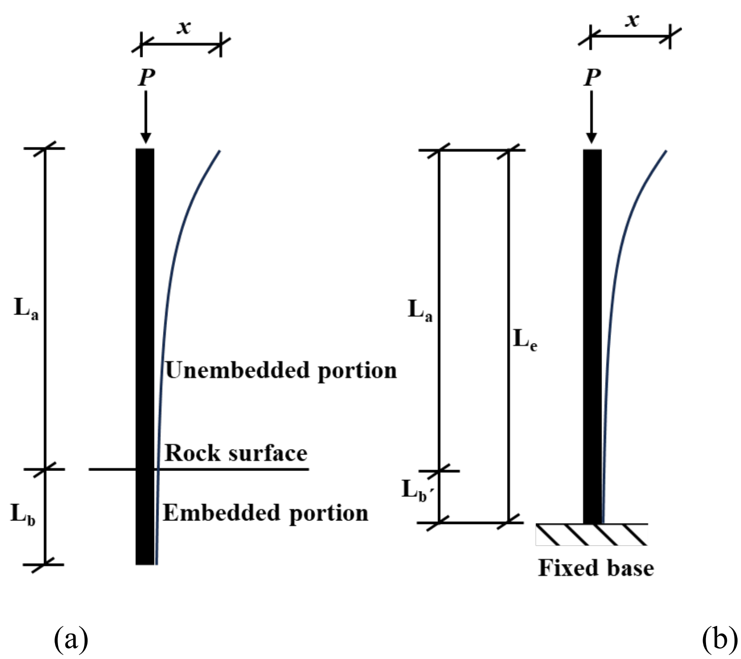

Fig. 16. Partially embedded pile system: (a) actual pile, and (b) equivalent system based on (after Heelis et al., 2004)